3-31-2011

In Vivo Tissue Diagnosis for Myocardial Infarction Using Optical Spectroscopy with Novel Spectral Interpretation Algorithms

Po-Ching Chen
Florida International University, pchen004@fiu.edu

FLORIDA INTERNATIONAL UNIVERSITY

Miami, Florida

IN VIVO TISSUE DIAGNOSIS FOR MYOCARDIAL INFARCTION USING

OPTICAL SPECTROSCOPY WITH NOVEL SPECTRAL INTERPRETATION

ALGORITHMS

A dissertation submitted in partial fulfillment of the

requirements for the degree of

DOCTOR OF PHILOSOPHY

in

BIOMEDICAL ENGINEERING

by

Po-Ching Chen

2011

To: Dean Amir Mirmiran
     College of Engineering and Computing

This dissertation, written by Po-Ching Chen, and entitled In Vivo Tissue Diagnosis for Myocardial Infarction using Optical Spectroscopy with Novel Spectral Interpretation Algorithms, having been approved in respect to style and intellectual content, is referred to you for judgment.

We have read this dissertation and recommend that it be approved.

_____
Armando Barreto

_____
Anthony McGoron

_____
Richard Bone

_____
Yen-Chih Huang

_____
Wei-Chiang Lin, Major Professor

Date of Defense: March 31, 2011

The dissertation of Po-Ching Chen is approved.

_____
Dean Amir Mirmiran
College of Engineering and Computing

_____
Dean Kevin O'Shea
University Graduate School

Florida International University, 2011

ACKNOWLEDGMENTS

ABSTRACT OF THE DISSERTATION

IN VIVO TISSUE DIAGNOSIS FOR MYOCARDIAL INFARCTION USING

OPTICAL SPECTROSCOPY WITH NOVEL SPECTRAL INTERPRETATION

by

Po-Ching Chen

Florida International University, 2011

Miami, Florida

Professor Wei-Chiang Lin, Major Professor

In recent decades, the rapid development of optical spectroscopy for tissue diagnosis has been indicative of its high clinical value. The goal of this research is to prove the feasibility of using diffuse reflectance spectroscopy and fluorescence spectroscopy to assess myocardial infarction (MI) in vivo. The proposed optical technique was designed to be an intra-operative guidance tool that can provide useful information about the condition of an infarct for surgeons and researchers.

In order to gain insight into the pathophysiological characteristics of an infarct, two novel spectral analysis algorithms were developed to interpret diffuse reflectance spectra. The algorithms were developed based on the unique absorption properties of hemoglobin for the purpose of retrieving regional hemoglobin oxygenation saturation and concentration data in tissue from diffuse reflectance spectra. The algorithms were evaluated and validated using simulated data and actual experimental data.

Finally, the hypothesis of the study was validated using a rabbit model of MI. The mechanism by which the MI was induced was the ligation of a major coronary artery of the left ventricle. Three to four weeks after the MI was induced, the extent of myocardial

tissue injury and the evolution of the wound healing process were investigated using the proposed spectroscopic methodology as well as histology. The correlations between spectral alterations and histopathological features of the MI were analyzed statistically.

The results of this PhD study demonstrate the applicability of the proposed optical methodology for assessing myocardial tissue damage induced by MI in vivo. The results of the spectral analysis suggest that connective tissue proliferation induced by MI significantly alter the characteristics of diffuse reflectance and fluorescence spectra. The magnitudes of the alterations could be quantitatively related to the severity and extensiveness of connective tissue proliferation.

TABLE OF CONTENTS

LIST OF TABLES

1. Background

1.1. Myocardial infarction

According to the statistics [1], 8.3 millions of American adults suffered myocardial infarction (MI) or heart attack in 2007. To date, MI is the major cause of death in coronary heart diseases. Acute MI results in $31 billion in hospital charges for 695,000 hospital stays [1].

MI is the occlusion of the coronary artery which depresses the blood supply to certain parts of the heart. The subsequent shortage of the blood perfusion, ischemia, reduces the oxygen supply. When the blockage is severe, it can cause myocardium impairment or cell death. The major cause of MI is the luminal thrombus in the coronary artery, and is usually from the rupture of a vulnerable atherosclerotic plaque on the artery wall. The build up of the atherosclerotic plaque begins from a high low-density-lipoprotein-cholesterol (LDLC) concentration in the plasma. Then the high-level LDLC accumulates under the intima and leads to a series of inflammatory processes in the arterial wall where macrophages release enzymes that transform stable plaques to vulnerable plaques.

Myocardial ischemia firstly converts aerobic metabolism to anaerobic metabolism, which reduces the oxidative phosphorylation in the electron transport system within seconds and reduces the adenosine triphosphate (ATP) production. This situation increases glycolysis with impaired pyruvate oxidation and converts pyruvate to lactate, causing more glucose uptake, more glycogen breakdown, an elevated lactate content, and a drop of pH in the cell. This process severely disturbs the homeostasis of the cell.

Meanwhile, under moderate ischemia, the slow oxidative phosphorylation introduces the decrease in flavin adenine dinucleotide (FAD), the accumulation of nicotinamide adenine dinucleotide (NADH) and a raised NADH to NAD$^+$ ratio [2].

1.1.1. Evolution of non-reperfused myocardial infarction

When the shortage of the oxygen supply continues, the ischemic myocytes lose their contractility in sixty seconds because of a reduced ATP production [3]. When the ischemic condition is severe and prolonged, the ischemic injury can become irreversible. If the occlusion of the blood flow persists for twenty to forty minutes, the injured myocytes will progress to cell death [3, 4]. Two basic types of cell death, oncosis and apoptosis, are found under irreversible ischemic damage [5]. Oncosis results in cell swelling which is associated with the failure of the ion transport system and a progressive damage of the cell membrane (sarcolemma) [5-7]. Apoptosis, a high energy dependent process results in cell shrinkage and is also found in ischemic injury especially after reperfusion. The rate of ATP depletion determines whether the irreversibly injured cell performs oncosis or apoptosis [7] . The current understanding is that the two cell death processes, oncosis and apoptosis, occur in parallel after MI. The majority of myocyte death occurs in subendocardium region at forty to sixty minutes after severe ischemia, progresses into subepicardium as a wave front phenomenon and completes the expansion of bed-at-risk within three to four hours [4, 6].

Hypereosinophilia of myocytes could be the earliest microscopic finding of myocardial infarction that can be discerned about12 to 24 hours after onset of chest pain. The appearance of wavy fibers may be discerned due to the result of stretching of

noncontractile fibers by the adjacent contracting myocytes. The necrotic cellular debris triggers the acute inflammatory reaction which initially induces an influx of neutrophils at 24 to 48 hours after occlusion [8-10]. Coagulation necrosis is developed with various levels of nuclear pyknosis, early karyorrhexis, and karyolysis at the same time. The loss of myocyte striations and nuclei is shown at 3 to 5 days [11]. Then, at 7 days, the infiltration of lymphocytes and macrophages ensue to clean up the dead myocytes with a significant decrease in neutrophils [8, 10] . Within the second week, the infarcted tissue has prominent angiogenesis and a high proliferation of fibroblasts along with deposit of collagen [3]. These processes develop granulation tissue which is rich in inflammatory cells and fibroblasts. Neocapillary and collateral blood flow are found abundant in granulation tissue [8, 12].

The granulation tissue formation reaches its highest level in 14 days. After that, the healing process continues and it converts granulation tissue into scar tissue. Consequently, the cell number declines in the infarcted region through apoptosis. The complete healing requires weeks or longer. However, there is a persistent presence of fibroblasts even after maturation of scar tissue, which is a unique phenomenon in cardiac scar [13].

The wound healing process post MI might have a different course depending on different species, the size of infarct, collateral blood flow, and various local and systemic factors [14, 15]; however, the evolution of MI follows a similar pattern [16].

1.2. Optical Spectroscopy for tissue diagnosis

The rapid development of optical spectroscopy for tissue diagnosis in recent decades demonstrates the high clinical value of this technique [17]. The basic concept of this technology is to investigate the cellular level activities in tissues by analyzing the interaction between the light and biomolecules. This technique has been successfully applied to diagnose a variety of tissues [18-22]. Further, this modality exhibits a number of advantages in terms of high safety, non-ionizing, non-invasive, high efficiency, high sensitivity, real-time, portability, and economy. In this proposal, two types of optical spectroscopies, diffuse reflectance spectroscopy and fluoresced spectroscopy, are utilized for MI diagnosis.

1.2.1. Diffuse reflectance spectroscopy

Diffuse reflectance spectroscopy aims to determine the absorption and scattering from the biological tissue. The major chromophores in the tissue are proteins, hemoglobin (Hb), myoglobin (Mb), water, and melanin [23]. Because each chromophore has distinct absorption properties in different wavelength regions, the chromophores can be identified and quantified individually.

Hb and Mb have nearly identical spectral properties in the visible and the near infrared regions [24] and their absorption spectrum is dominant within 450nm to 600nm. This spectral characteristic has been widely used to gauge blood and oxygen perfusion in the tissue [25-27]. The absorption of oxy-Hb is higher than that of deoxy-Hb at certain wavelengths (e.g. 576 nm) but is lower at other wavelengths (e.g. 560 nm). Hence, the ratio of diffuse reflectance spectra at two carefully selected wavelengths is a good

reference for measuring the relative variation in oxygen saturation ($SatO_2$) of Hb and Mb. The absorption of oxy-Hb and deoxy-Hb are identical at several specific wavelengths known as the isosbestic wavelengths (e.g. 449 nm, 548 nm , and 568 nm). Diffuse reflectance spectra at these isosbestic wavelengths are insensitive to $SatO_2$ and can be used for estimating relative Hb and Mb concentration in the tissue

In the spectral region beyond 700nm where the absorption from Hb and Mb is relatively low, the diffuse reflectance spectrum can be used to assess tissue scattering properties. The scattering event is related to the density and the size of the scatters which directly associate with the structural and morphological characteristics of the tissue. Many studies suggest that abnormal tissues such as tumors or cancers have obvious changes in their respective scattering properties [28, 29].

1.2.2. Fluorescence spectroscopy

Fluorescence spectroscopy is another commonly used optical approach for tissue diagnosis. At 337 nm excitation, the biological fluorophores contributing significantly to the overall tissue autofluorescence are elastin, collagen, NADH and FAD, and their maximum emission wavelengths are 400nm, 405nm, 460nm and 535nm respectively [30].

NADH and FAD are intrinsic biological fluorophores which are significantly correlated with tissue metabolism. When the metabolism slows down, the accumulation of NADH and the reduction of FAD occur. Therefore, fluorescence spectra can be very useful to analyze the relative changes in the metabolic status. Collagen and elastin are structural proteins which are good indicators for assessment of tissue fibrosis. The

applicability for tissue damage estimation through fluorescence spectroscopy has been proven in several different studies [30-34].

2. Significance and goals

The current *in vivo* imaging modalities - like contrast-enhanced magnetic resonance imaging (cMRI), positron emission tomography, (PET) and single-photon emission computed tomography (SPECT) - have limitations for estimating myocardial tissue damage [35-39]. Especially, it has been expensive and challenging to adapt these methodologies into intraoperative applications.

A new diagnostic apparatus is proposed for intraoperative myocardial tissue characterization, incorporating diffuse reflectance spectroscopy and fluorescence spectroscopy. The primary goal of this PhD research is to demonstrate the feasibility of the developed diagnostic apparatus in characterizing *in vivo* physiological alterations (local tissue hemodyanics and metabolism) and pathological alterations (local tissue microscopic morphology) in myocardium induced by myocardial infarction (MI). This innovative apparatus may be used during bypass graft surgery or myocardium transplantation as a surgical guidance tool, providing surgeons and researchers useful information including local myocardial tissue conditions post infarction, and the evaluation of microvascular perfusion and tissue oxygenation surrounding an infarct in real-time.

Two major aims listed below describe the procedures of accomplishing the goal of this PhD research project.

Aim 1: To derive two novel spectral interpretation algorithms that estimate regional hemoglobin oxygenation saturation and concentration respectively from *in vivo* tissue

using diffuse reflectance spectra, and to validate the proposed algorithms using simulated spectra, tissue phantoms, and clinical data.

Aim 2: To design and improve a spectroscopy system that acquires *in vivo* diffuse reflectance and fluorescence spectra, and to demonstrate the feasibility of using combined diffuse reflectance spectroscopy and fluorescence spectroscopy to evaluate post MI injury using a rabbit model.

3. A new algorithm for hemoglobin oxygen saturation determination from diffuse reflectance spectra

3.1. Introduction

The microcirculation is that part of the vascular tree that comprises blood vessels smaller than 100 μm in diameter, including arterioles, capillaries, and venules. One of its primary roles is to distribute oxygen throughout tissues. The main oxygen carrier within the circulatory system is red blood cells (RBCs), and the oxygen transport rate in various organs is controlled by microvascular geometry, hemodynamics, and RBC hemoglobin (Hb) oxygen saturation. Since diseases and injuries can lead to certain local modifications in microvasculature, and hence microvascular oxygen transport, local tissue may be hypoxic despite normal global Hb oxygenation. For example, sepsis leads to the termination of flow in a significant number of capillaries, such that the microcirculation fails to compensate for decreased functional capillary density [40]. This change elevates the likelihood of local organ failure. Furthermore, the steady state level of Hb oxygenation in the microcirculation represents the balance between cellular O_2 consumption and the supply of oxygenated blood. This, in turn, provides indirect access to the metabolic characteristics of local tissue, an important physiological indicator of tissue viability. Therefore, understanding and assessing Hb oxygenation in the microcirculation provides valuable insights into a given patient's level of health. It is not surprising, then, that local Hb oxygenation is highly-sought information in medical research, as well as in clinical care [41-46].

Common *in vitro* Hb oxygenation sensors can be divided into two categories: electrochemical sensors and optical sensors. In the field of medicine, the optical sensors often are selected because of their non-destructive and/or non-invasive nature. The optical sensors utilize the oxygenation-dependent absorption properties of Hb to quantify its oxygenation. Depending upon its implementation, transmitted light at two or more wavelengths will be captured. When the assumptions of constant Hb concentration and optical pathlength are valid, a simple Beer-Lambert law may be used to convert light attenuation to the relative absorption properties of Hb and, hence, Hb oxygenation. A conventional CO-oximeter is typical of such an approach [47].

Accurately measuring Hb oxygenation from *in vivo* tissue is a difficult task because biological tissues are highly scattering. In addition, diffusely reflected light signals (i.e., diffuse reflectance spectroscopy) often are measured because of several limitations imposed by tissue geometry and measurement environment. These two conditions, collectively, complicate the process of assessing *in vivo* Hb oxygenation; scattering-induced light attenuation and pathlength alteration have to be considered by the photon migration model that converts diffuse reflectance signals to optical properties and then to Hb oxygenation. Several groups have the modified Beer-Lambert law either empirically or theoretically to accommodate those scattering induced effects [48-52]. More sophisticated models have been proposed, including the diffuse approximation model [53], the Monte Carlo (MC) based inverse model [54], the mathematical approximation model [26], and the empirical model [29, 55]. Within these models, a set of coefficients is used to define a diffuse reflectance spectrum, and these coefficients are adjusted systematically until the model-predicted diffuse reflectance spectrum closely

resembles the one actually measured. From the optimal coefficients, the absorption properties of the measured subject can be estimated and its Hb oxygenation determined. One shortcoming of these approaches is that they require a series of rigorous intensity calibrations against tissue phantoms or references to assure the estimate accuracy.

In this article, we propose a new algorithm that estimates Hb oxygenation by analyzing the Hb oxygenation-induced spectral profile alterations in diffuse reflectance spectra within the visible wavelength region. The algorithm is applicable to various tissue types (i.e., scattering properties) and can be used in conjunction with a diverse range of probe geometries for real-time monitoring of Hb oxygenation.

3.2. Method and theory

The Hb oxygenation extraction algorithm proposed in this study was developed based on an important absorption characteristic of Hb: the profile of the extinction coefficient spectrum of Hb from 450 nm to 600 nm alters drastically between the oxygenated and the deoxygenated states. The extinction coefficient spectrum of Hb at a given oxygen saturation ($SatO_2$) level can be calculated using Eq. (3.1).

$$\varepsilon^{SatO2}(\lambda) = SatO_2 \cdot \varepsilon^{oxy}(\lambda) + (1 - SatO_2) \cdot \varepsilon^{deoxy}(\lambda) \text{ [liter/mole/cm]}, \quad (3.1)$$

where λ is wavelength [nm], $\varepsilon^{oxy}(\lambda)$ is the extinction coefficient spectrum of oxy-Hb [liter/mole/cm], and $\varepsilon^{deoxy}(\lambda)$ is the extinction coefficient spectrum of deoxy-Hb [liter/mole/cm]. When comparing $\varepsilon^{SatO_2}(\lambda)$ at various $SatO_2$ levels, it clearly shows that $SatO_2$ level influences both the spectral feature types (e.g., peaks and valleys) as well as their locations in $\varepsilon^{SatO2}(\lambda)$. Therefore $SatO_2$ information may be extracted from

11

$\varepsilon^{SatO2}(\lambda)$ by quantifying the location of a specific spectral feature in $\varepsilon^{SatO2}(\lambda)$, which is the central theorem of the proposed Hb oxygenation extraction algorithm.

To facilitate the identification and localization of a specific spectral feature in $\varepsilon^{SatO2}(\lambda)$, a differential wavelet transform (DWT) technique was employed in the Hb oxygenation extraction algorithm. DWT of $\varepsilon^{SatO2}(\lambda)$ is denoted by $W_s^n \varepsilon^{SatO2}(u)$ where u is a translation, s is a scale parameter, and n is a differential parameter. From a signal processing point of view, DWT is equivalent to filtering; the input signal (i.e, $\varepsilon^{SatO2}(\lambda)$) is filtered by a linear band-pass filter with a passing band controlled by s. In the algorithm, DWT removes those unwanted frequency components from the input signal (i.e., processed signal) and makes the spectral features more identifiable. The detailed definition and explanation of DWT can be found in 3.8 Appendix. Here various n values were used in DWT to identify different spectral feature types in $\varepsilon^{SatO2}(\lambda)$; zero-crossing points of $W_s^n \varepsilon^{SatO2}(u)$, denoted by $Z_{j,s,n}^{\varepsilon}$, were used to localize these features [56]. Specifically, $Z_{j,s,n=1}^{\varepsilon}$ locates the j-th local maximum or minimum in filtered $\varepsilon^{SatO2}(\lambda)$; $Z_{j,s,n=2}^{\varepsilon}$ locates the j-th inflection point; $Z_{j,s,n=3}^{\varepsilon}$ locates the j-th local maximum curvature. Based on the central theorem mentioned above, the variations of $Z_{j,s,n}^{\varepsilon}$ (i.e., movements of the spectral features in $\varepsilon^{SatO2}(\lambda)$) should be strongly related to the $SatO_2$ level of Hb. This relationship can be formulated by a function $S_{j,s,n}$ that is written as:

$$SatO_2 = S_{j,s,n}(Z_{j,s,n}^{\varepsilon}) \ [\%]. \qquad (3.2)$$

In order to apply the relationship derived in Eq. (3.2) to diffuse reflectance spectra, preprocessing of diffuse reflectance spectra is necessary. According to the theory of

photon migration, absorption events reduce the weight of a photon package during the migration process. Therefore, the remaining energy of a diffusely reflected photon package may be described as:

$$E(r,\lambda) = E_0(r_0,\lambda)e^{-\mu_a(\lambda)\cdot l(r,\lambda)} \text{ [J]}, \qquad (3.3)$$

where r is the distance between the source and detector [cm], E_0 is the initial energy of the photon package [J], r_0 is the entrance point of the photon package (i.e., source location), $E(r,\lambda)$ is the remaining energy of the photon package [J] when it remerges at r, $\mu_a(\lambda)$ is the absorption coefficient of the medium [1/cm], and $l(r,\lambda)$ is the migration pathlength of the photon package [cm]. Note that $l(r,\lambda)$ is a function of the reduced scattering properties of the medium $\mu_s'(\lambda)$ [1/cm] as well as r. A steady-state diffuse reflectance signal $Rd(r,\lambda)$ [W], therefore, is the sum of the all escaped photons at a given surface location per unit time. That is:

$$Rd(r,\lambda) = \frac{\sum_{i=1}^{x} E_i(r,\lambda)}{T} = \frac{E_0(r,\lambda)}{T}\sum_{i=1}^{x}e^{-\mu_a(\lambda)\cdot l_i(r,\lambda)} \approx \frac{E_0(r,\lambda)}{T}e^{-\mu_a(\lambda)\cdot k(r,\lambda)} \text{ [W], (3.4)}$$

where x is the number of diffusely reflected photon packages remerged at r, T is the time to deliver the entire incident photon packages, $k(r,\lambda)$ is a constant calculated from $k(r,\lambda) = -\ln(\sum_{i=1}^{x}e^{-\mu_a(\lambda)\cdot l(r,\lambda)})/\mu_a(\lambda)$. Based on this theory, a natural logarithmic operation could be applied to $Rd(r,\lambda)$ to obtain the absorption characteristics (i.e., $\mu_a(\lambda)$) and the scattering characteristics (i.e., $k(r,\lambda)$). Assuming Hb is the only dominant chromophore of biological tissues between 450 nm and 600 nm and the spectral profile of $k(r,\lambda)$ is relatively monotonic, the spectral profile of $-\ln[Rd(r,\lambda)]$ between

13

450 nm and 600 nm should strongly resemble that of $\varepsilon^{SatO2}(\lambda)$ within the same spectral region.

To effectively detect the spectral profile alterations in $-\ln[Rd(r,\lambda)]$ induced by $SatO_2$ variations, DWT was again used on $-\ln[Rd(r,\lambda)]$. The transformed $-\ln[Rd(r,\lambda)]$ is denoted by $W_s^n\{-\ln[Rd(r,u)]\}$. The locations of the spectral features in $-\ln[Rd(r,\lambda)]$ are tracked by the zero-crossing points in $W_s^n\{-\ln[Rd(r,u)]\}$, which are denoted by $Z_{j,s,n}^{Rd}$. In the extraction algorithm, it is assumed that $Z_{j,s,n}^{\varepsilon}$ acquired from the extinction spectra should be coincided with $Z_{j,s,n}^{Rd}$. Therefore, $S_{j,s,n}$ in Eq. (3.2) can be used as the lookup functions to estimate the $SatO_2$ level in $Rd(r,\lambda)$ using $Z_{j,s,n}^{Rd}$ as the inputs. That is:

$$SatO_{2\,j,s,n}^{est} = S_{j,s,n}(Z_{j,s,n}^{Rd}) \ [\%]. \ (3.5)$$

3.3. Algorithm validation and evaluation using Monte Carlo simulation

To validate the proposed algorithm, an extensive diffuse reflectance spectra database was created using a MC simulation model of photon migration. In the simulation model, a semi-infinite medium with homogenous optical properties was used to mimic a biological tissue. In each simulation, a total of three million photons were injected into the medium at the origin (i.e., $(r,z) = (0,0)$). The energy of reflected photons was recorded as a function of the exit position r in order to create the diffuse reflectance spectra $Rd_{sim}(r,\lambda)$. Note that the exit angles of the reflected photons were not recorded in the database.

In the MC simulation model, the only absorber used was Hb due to its dominant nature within the spectral region of 450 nm to 600 nm in biological media. The absorption property of the simulated medium hence was defined by the following equation:

14

$$\mu_a(\lambda) = BVF[\overline{SatO_2} \times \mu_a^{oxy}(\lambda) + (1 - \overline{SatO_2}) \times \mu_a^{deoxy}(\lambda)] \ [1/cm], \qquad (3.6)$$

where BVF is the blood volume fraction [%], $\overline{SatO_2}$ is the user-defined $SatO_2$ level of Hb

[%], $\mu_a^{oxy}(\lambda)$ is the absorption coefficient of oxygenated blood [1/cm], and $\mu_a^{deoxy}(\lambda)$ is

the absorption coefficient of deoxygenated blood [1/cm]. $\mu_a^{oxy}(\lambda)$ and $\mu_a^{deoxy}(\lambda)$ were

obtained from $\varepsilon^{oxy}(\lambda)$ and $\varepsilon^{deoxy}(\lambda)$, respectively, with the whole blood Hb concentration

of 150 gram/liter. The reduced scattering coefficients in biological tissue were

approximated by the following equation [53, 57]. That is:

$$\mu_s'(\lambda) = A \times w^{-B} \ [1/cm], \qquad (3.7)$$

where $w = \lambda \times 10^3$. The ranges of all variables associated with the optical properties are

summarized in Table 3-1. Note that the ranges of the optical properties used to construct

$Rd_{sim}(r,\lambda)$ encompass the majority of biological tissue types and hemodynamic

conditions [58]. Furthermore, $Rd_{sim}(r,\lambda)$ was recorded from r = 0.0075 cm to r =

0.9975 cm, which covers the source-detection separations commonly used in the *in vivo*

diffuse reflectance spectroscopy studies.

Table 3-1 Variables used in constructing $Rd_{sim}(r,\lambda)$ and their ranges used.

Variable	Start Value	Increment	End Value
r	0.0075 cm	0.005 cm	0.9975 cm
BVF	1 %	1 %	8 %
$SatO_2$	0 %	10 %	100 %
A	600	200	1400
B	0.9	0.2	1.5
λ	400 nm	2 nm	650 nm

To retrieve the *SatO₂* information from $Rd_{sim}(r,\lambda)$, the algorithm described in the previous section was applied to $Rd_{sim}(r,\lambda)$. The performance of the algorithm was evaluated by calculating the absolute error between the actual and the estimated *SatO₂* levels. That is:

$$SatO_{2j,s,n}^{error} = \left| \overline{SatO_2} - SatO_{2j,s,n}^{est} \right| \ [\%], \ (3.8)$$

where $\overline{SatO_2}$ is the actual *SatO₂* level of the Hb used in the MC simulations, as defined in Eq. (3.6), and $SatO_{2j,s,n}^{est}$ is the estimated *SatO₂* level of Hb derived from the extraction algorithm using Eq. (3.5). $SatO_{2j,s,n}^{error}$ was calculated with extended combinations of *(j,s,n)*. The $S_{j,s,n}$, as defined in Eq. (3.5), producing the lowest mean $SatO_{2j,s,n}^{error}$ over the entire range of the simulation parameters was identified as the ideal lookup function to retrieve the *SatO₂* level of Hb from a diffuse reflectance spectrum using the proposed algorithm.

3.4. Algorithm validation and evaluation using *in vivo* experiments

To demonstrate its clinical utility, the proposed Hb oxygenation extraction algorithm was applied to the diffuse reflectance spectra acquired from *in vivo* tissue, using a fiber-optic spectroscopy system. The system utilized a tungsten-halogen lamp (LS-1, Ocean Optics, Dunedin, FL) as the excitation source and a spectrometer (USB 2000, Ocean Optics, Dunedin, FL) to record diffuse reflectance spectra. A fiber-optic probe was employed for excitation light delivery and reflected light collection. All the experimentally-acquired diffuse reflectance spectra were calibrated against a standard (FGS-20-02c, Avian Technologies, NH, USA), so as to remove the spectral profile alterations induced by the spectroscopy system, and then re-sampled to reduce the spectral data interval to 2 nm.

In the first *in vivo* experiment, the algorithm was used to extract the local Hb oxygenation information at a fingertip under normal and ischemic conditions. The fiber-optic probe used in this experiment consisted of three 600 μm core-diameter optical fibers: one was used for excitation and the other two (fiber A and fiber B) for detection. The distances between the center of the excitation fiber and those of the detection fibers were 810 μm for fiber A and 1116 μm for fiber B. During the experiment, the probe was placed in direct contact with the fingertip, using a probe holder, to maintain stability of the contact position and pressure. Two spectrometers were used to acquire the diffuse reflectance spectra from the two detection fibers separately and simultaneously. A short-term local ischemic condition of the fingertip was created by tightening a rubber band placed at the base of the finger to reduce blood flow for 400 seconds. Diffuse reflectance spectra were acquired continuously at the rate of 0.5 Hz (1) prior to the occlusion to establish a normal reference, (2) during the ischemia and (3) after releasing the rubber band.

In the second *in vivo* experiment, the algorithm was applied to diffuse reflectance spectra measured from the *in vivo* brains of six pediatric patients who were undergoing a craniotomy for brain tumor recession. The clinical study was conducted in accordance with a protocol approved by the Western Institutional Review Board and the Institutional Review Board of Florida International University, with consent from the patients and their parents. Methodological details of this *in vivo* study have already been published [59]. The fiber-optic probe used consisted of seven 300 μm optical fibers; one was used for excitation, one remained unused, and the remaining five were utilized for detection. The average source-detector separation distance was about 460 μm. The probe was held by the surgeon and placed in direct contact with the brain tissue. For each patient study,

diffuse reflectance spectra were collected at a rate of 33 Hz for 12 seconds from normal cortex (i.e., outside the resection zone) and from the tumor (later confirmed by histology).

3.5. Spectral signal quality evaluation

MC simulation is a statistical-based model and requires a large number of repetitions (i.e., input photons) to reduce the statistical noises. Hence diffuse reflectance spectra acquired by both *in vivo* experiments and MC simulation inevitably contain noises. For this reason, the noise level of $-\ln[Rd(r,\lambda)]$ and its impacts on the performance of the Hb oxygenation extraction algorithm were evaluated. To accomplish this goal, the signal to noise ratios *(S/N)* of $-\ln[Rd(r,\lambda)]$ had to be defined first. As mentioned previously, DWT is equivalent to band-pass filtering. With *s*=1, DWT of $-\ln[Rd(r,\lambda)]$ isolates the highest frequency component in $-\ln[Rd(r,\lambda)]$, which is treated as the noise component. Therefore, depending on the *s* and *n* parameters used in DWT, *S/N* of a transformed $-\ln[Rd(r,\lambda)]$ with $s > 1$ can be conveniently estimated using the following equation:

$$S/N(s,n) = \frac{\left| \sum_{u=540}^{560} W_s^n \{-\ln[Rd(r,u)]\} \right|^2}{\left| \sum_{u=540}^{560} W_1^n \{-\ln[Rd(r,u)]\} \right|^2}. \qquad (3.9)$$

3.6. Results

According to Table 3-1, the database of $Rd_{sim}(r,\lambda)$ consists of 350240 spectra. During the evaluation and the validation, however, some spectra, especially those with large source-detector separations *r*, were considered as unusable because they contained zero

data points (i.e., no signal). The average *S/N* of transformed $Rd_{sim}(r, \lambda)$ at each *r* was used to evaluate this phenomenon. It was found that the number of unusable spectra increases and the *S/N* of transformed spectra decreases when *r* exceeds 0.3 cm. Figure 3-1 demonstrates two examples of the average *S/N* versus number of unusable spectra at various *r* with different *s* and *n* combinations. In order to avoid the errors induced by poor *S/N* over the majority of optical property ranges defined in Table 3-1, the following evaluation and validation were carried out for $r \leq 0.3$ cm only. This limitation results in a total of 103840 spectra, 9440 spectra per $SatO_2$ level, and 1760 at each *r* in the reduced $Rd_{sim}(r, \lambda)$ database.
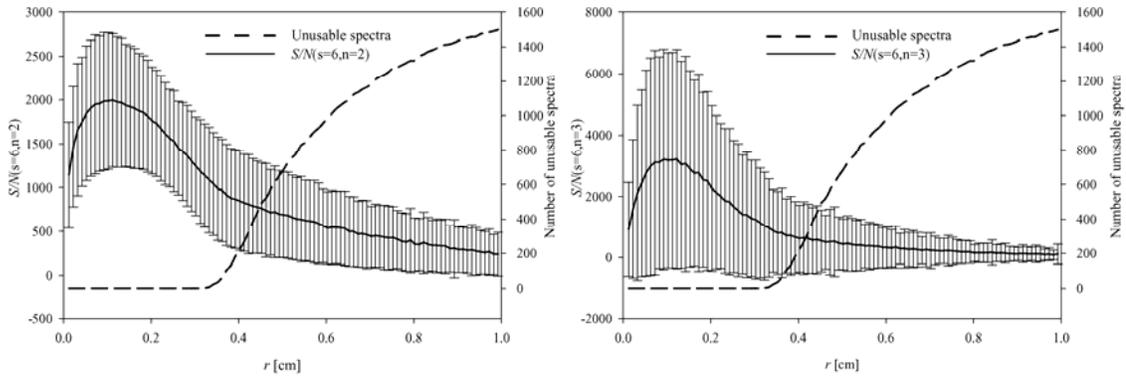
Figure 3-1. The correlation between the number of unusable spectra and *S/N*(s,n) at various *r*. The long dash line represents the number of unusable spectra in $Rd_{sim}(r, \lambda)$. The solid curve is the mean *S/N* of transformed $Rd_{sim}(r, \lambda)$, and the error bars represent the standard deviations.

Search of the ideal $S_{j,s,n}$ for the proposed Hb oxygenation extraction algorithm was carried out using $n = 1$ to 3 and $s = 2$ to 9 in DWT of $Rd_{sim}(r, \lambda)$ within the spectral region of 450 nm to 600nm. The results of the search show that, among all (j,s,n) combinations, $(j,s,n) = (2,6,2)$ produces the minimal mean $SatO_{22,6,2}^{error}$ defined by Eq. (3.8).

This indicates that $S_{2,6,2}$ is the ideal lookup function for the proposed algorithm. According to Eq. (3.2), $S_{2,6,2}$ was constructed using the location of the second inflection point identified by $Z^{\varepsilon}_{2,6,2}$. Figure 3-2 (a) depicts how $Z^{\varepsilon}_{2,6,2}$ shifts in according with the spectral profile alteration in $\varepsilon^{SatO2}(\lambda)$ induced by $SatO_2$. This relationship was fitted nicely ($r^2 = 0.99$) by a rational decay function, $S_{2,6,2}$, as shown in Figure 3-3 (a). $Z^{Rd}_{2,6,2}$ retrieved from $Rd_{sim}(r,\lambda)$ at each $SatO_2$ level defined in Table 3-1 were also plotted in Fig 3 (a), which were found to follow the trend of $S_{2,6,2}$. This result verifies the validity as well as the accuracy of the proposed extraction algorithm.

It was also noted that in Figure 3-2 (a) $Z^{\varepsilon}_{2,6,2}$ vanishes when the $SatO_2$ level drops below 40 %. Therefore a second lookup function is required for low $SatO_2$ (i.e., < 40 %) in the proposed $SatO_2$ extraction algorithm. The results of the feature search and validation suggested that $S_{4,6,3}$ is the ideal lookup function to track low $SatO_2$ levels because it produced the minimal mean $SatO^{error}_{24,6,3}$ among all combinations evaluated. Figure 3-2 (b) depicts the correlation between $Z^{\varepsilon}_{4,6,3}$ and the $SatO_2$ induced spectral profile alterations in $\varepsilon^{SatO2}(\lambda)$. Similarly, this relationship was fitted nicely ($r^2=0.99$) using a 5th degree polynomial function, $S_{4,6,3}$, as shown in Figure 3-3 (b). $Z^{Rd}_{4,6,3}$ extracted from $Rd_{sim}(r,\lambda)$ at each $SatO_2$ level were also plotted in Figure 3-3 (b) which shows $S_{4,6,3}$ is a good lookup function for $Z^{Rd}_{4,6,3}$.
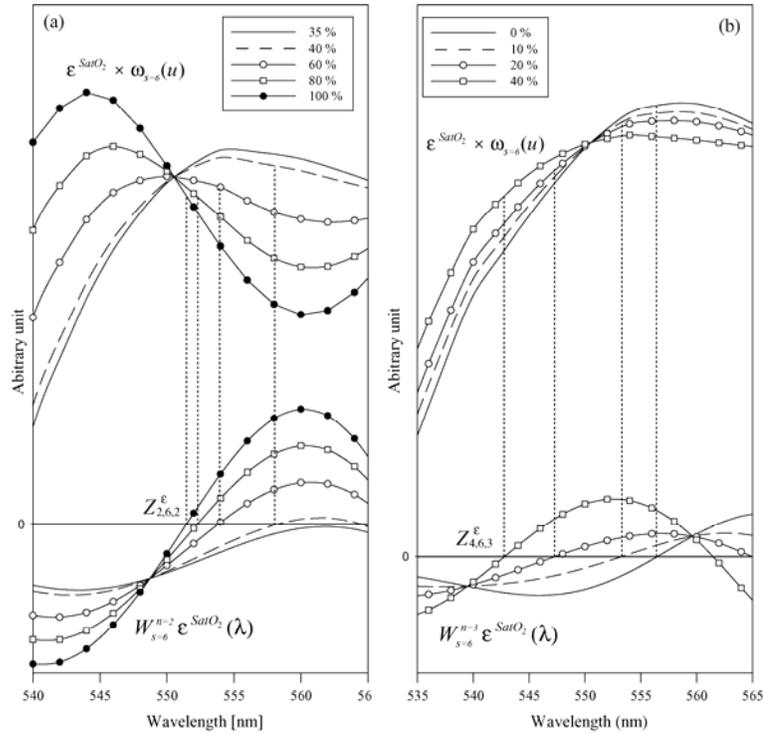
Figure 3-2. Panel (a) describes the effects of the *SatO₂* induced spectral profile alterations in $\varepsilon^{SatO2}(\lambda)$ on $Z_{2,6,2}^{\varepsilon}$ for *SatO₂* ≥ 40 %. The top and the bottom groups of curves represent the filtered $\varepsilon^{SatO2}(\lambda)$ and the DWT of $\varepsilon^{SatO2}(\lambda)$, respectively, at various *SatO₂* levels. The dot vertical lines show that the inflection points in the filtered $\varepsilon^{SatO2}(\lambda)$ are accurately localized by $Z_{2,6,2}^{\varepsilon}$. Panel (b) describes the similar capability of $Z_{4,6,3}^{\varepsilon}$ for *SatO₂* < 40 %
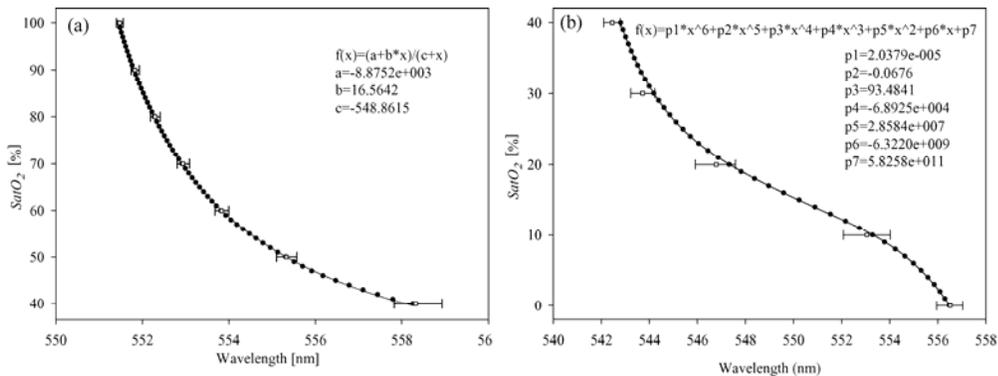
Figure 3-3. In panel (a), the solid dots show $Z_{2,6,2}^{\varepsilon}$ as a function of *SatO₂* (≥ 40 %). The solid line is the curve fit of all $Z_{2,6,2}^{\varepsilon}$ using a rational decay function, which

becomes the lookup function $S_{2,6,2}$. The empty squares represent the medians of $Z_{2,6,2}^{Rd}$ and the error bars represent the corresponding 10th and 90th percentiles. In panel (b), the solid dots are $Z_{4,6,3}^{\varepsilon}$ at various levels of *SatO₂* that are less than 40 %. The solid line is the curve fit of all $Z_{4,6,3}^{Rd}$ using a 5th order polynomial function, which becomes the lookup function $S_{4,6,3}$. The empty squares represent the medians of $Z_{4,6,3}^{Rd}$ and the error bars represent the corresponding 10th and 90th percentiles. These numbers are calculated from the entire reduced $Rd_{sim}(r,\lambda)$ database.**

Upon identifying the two ideal lookup functions, their corresponding estimation errors, namely $SatO_{22,6,2}^{error}$ and $SatO_{24,6,3}^{error}$, were used to evaluate the performance of the proposed Hb oxygenation extraction algorithm. The overall estimation error of the algorithm is 1.23 % ± 1.35 % (mean ± standard deviation) for the entire reduced $Rd_{sim}(r,\lambda)$ database.

Influences of individual variable defined in Table 3-1 on the performance of the algorithm also were individually evaluated. The analysis was carried out by calculating the estimation errors at all levels of one given variable, while the remaining variables were adjusted over the entire ranges.

The estimation errors at various *SatO₂* levels are shown in Figure 3-4 (a). The results indicate that the estimation errors are the highest at the *SatO₂* level of 30 %. This level is the transition point at which one lookup function is replaced by the other one to interpret the *SatO₂* level. The accuracy of the algorithm was also evaluated as a function of *BVF,* and the results are shown in Figure 3-4 (b). In general, the *SatO₂* estimation errors do not change significantly in accordance with the variations in *BVF*. The estimation error increases as the *BVF* level decreases; the highest estimation error (1.7 %) is found at *BVF* = 1 %.
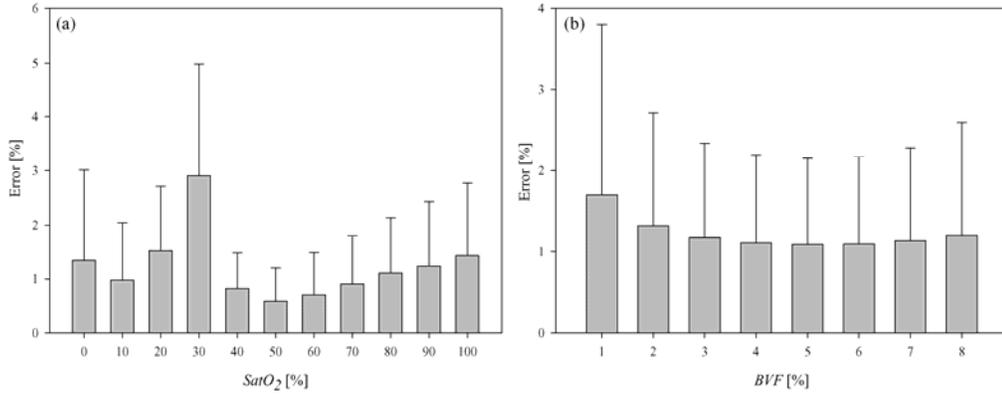
Figure 3-4. (a) *SatO₂*–dependence and (b) *BVF*-dependence of the *SatO₂* estimation errors. The solid bars represent the average estimation errors; the error bars represent the one standard deviation.

The *SatO₂* estimation errors were evaluated in according with the parameters *A* and *B*, which are used to define the reduced scattering coefficient $\mu'_s(\lambda)$ in Eq. (3.7). The outcomes, as shown in Figure 3-5, again suggest that the estimation errors are constant for all $\mu'_s(\lambda)$ levels.
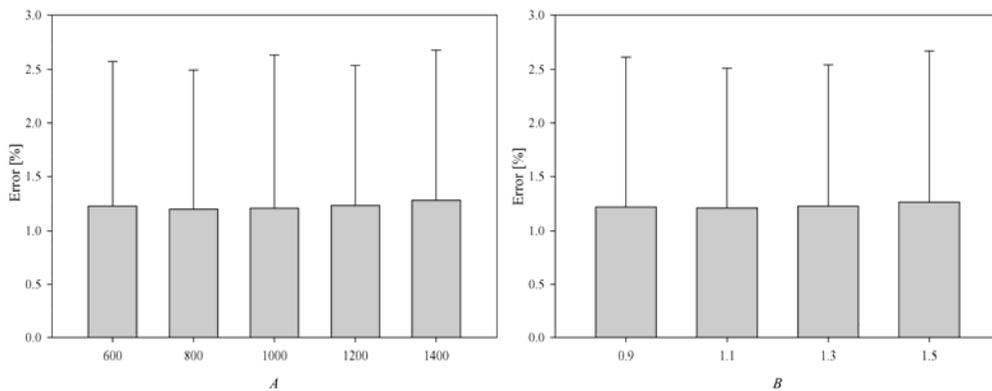
Figure 3-5. $\mu'_s(\lambda)$-dependence of the *SatO₂* estimation errors. The solid bars represent the average estimation errors; the error bars represent the one standard deviation.

As mentioned previously, the decision of choosing the ideal lookup functions and the evaluation of the algorithm were determined using the reduced $Rd_{sim}(r,\lambda)$ database

($r < 0.3$ cm). When applying this algorithm to the entire $Rd_{sim}(r,\lambda)$ database (i.e., $r = 0.0075$ cm to $r = 0.9975$ cm), the overall estimation error of the algorithm increases to 2.39 % ± 3.64 %. Figure 3-6 illustrates the estimation errors as a function of r, derived from the entire $Rd_{sim}(r,\lambda)$ database. As mentioned before, the number of usable spectra drops when r exceeds 0.3 cm. The estimation errors increase when r approaches the two extremes and the lowest estimation error was found between $r = 0.06$ cm to $r = 0.15$ cm.
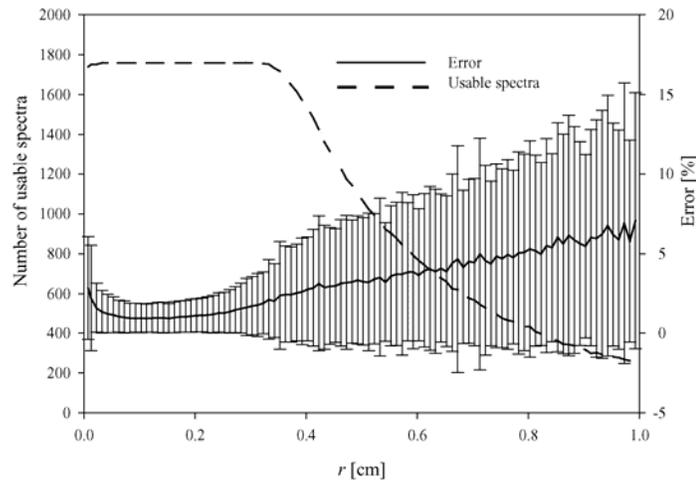
Figure 3-6. r-dependence of the $SatO_2$ estimation errors. The solid line represents the average estimation errors; the error bars represent the one standard deviation. The long dash line represents the number of usable spectra in $Rd_{sim}(r,\lambda)$.

Through the observations described above, it was found that the average estimation errors tend to increase when the mean S/N declines. To illustrate this negative correlation, the estimation errors were plotted against $S/N(2,6,2)$ for $SatO_2 \geq 40\%$ and $S/N(4,6,3)$ for $SatO_2 < 40\%$ respectively in Figure 3-7. Figure 3-7 also reveals that the average estimation errors rise above the overall estimation error when $S/N(2,6,2)$ for $SatO_2 \geq 40\%$ and $S/N(4,6,3)$ for $SatO_2 < 40\%$ descend below 700 and 70, respectively.
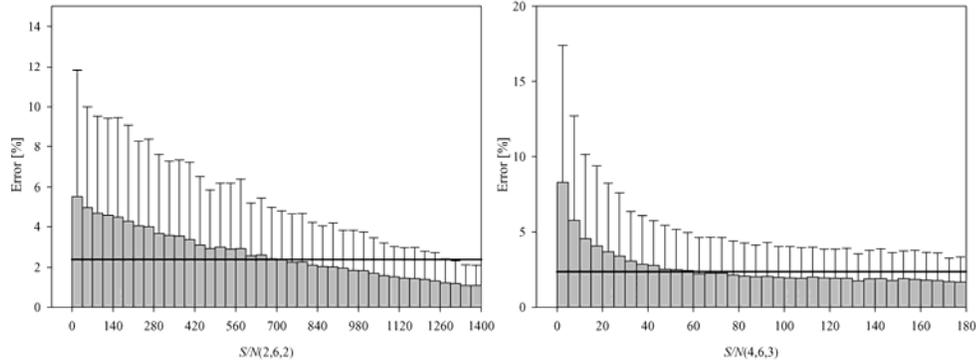
Figure 3-7. The relationship between the estimation errors versus *S/N*(2,6,2) **for** *SatO₂* $\geq$ 40% **and** *S/N*(4,6,3) **for** *SatO₂* < 40%. **The solid bars represent the average estimation errors within a specific range of** *S/N*; **the error bars represent the one standard deviation. The solid line represents the overall estimation error (2.39 %).**

For the *in vivo* fingertip ischemia experiment, the spectral data were taken from the tip of the middle finger of a volunteer (P. C.): the results are shown in Figure 3-8. The proximity of the two curves indicates that the *SatO₂* levels extracted using the diffuse reflectance spectra from the two detection fibers are fairly similar. For the first 400 seconds (normal reference), the average *SatO₂* level of the fingertip was 68.45% ± 2.55% from fiber A and 70.49% ± 2.55% from fiber B. The *SatO₂* level started to decline right after the rubber band was tightened and eventually plateaued. During the steady-state ischemic condition (i.e., 600 sec to 800 sec), the average *SatO₂* levels from fiber A and fiber B were 16.77% ± 2.90% and 17.01% ± 1.87%, respectively. The mean difference between fibers A and B was reduced during this period, relative to the normal reference level. The *SatO₂* level returned to normal range, as expected, once the rubber band was released.
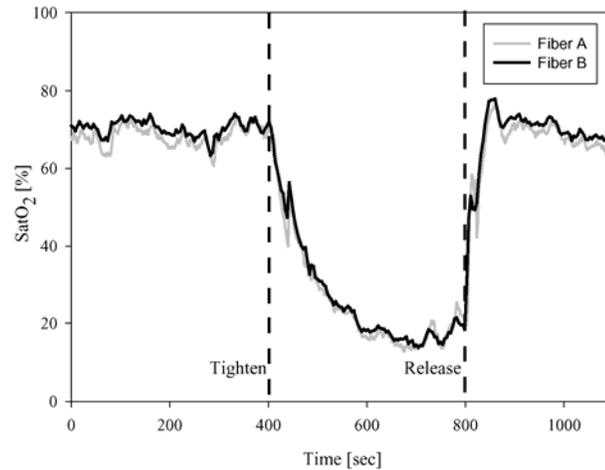
Figure 3-8. Time histories of local *SatO₂* variations at the fingertip during experimentally-induced ischemia. The *SatO₂* levels were derived from the diffuse reflectance spectra, recorded through fiber A and fiber B, using the proposed algorithm.

The demographic and histological information of the six brain tumor patients who participated in the clinical study are provided in Table 3-2. Figure 3-9 represents the estimated *SatO₂* level by the algorithm for each patient in normal cortex and the tumor area within the 12 second acquisition period. Figure 3-9 illustrates how the *SatO₂* level may fluctuate during acquisition. However, in general, normal cortex exhibited relatively higher *SatO₂* levels than tumor areas within the same patient. The average *SatO₂* level of the six patients was 66.42% ± 8.86% within normal cortex and 50.89% ± 13.09% in brain tumor. The *S/N* of all the experimental spectra were evaluated using Eq. (3.9) and found above the threshold depicted in Figure 3-7.

Table 3-2. Demographic data on the 6 patients who participated in the clinical study

Case #	Gender	Age	Tumor type
1	M	1	PNET
2	F	9	PNET
3	M	10	Pilocytic astrocytoma
4	F	5	Angioglioma
5	F	6	Astrocytoma
6	F	9	Astrocytoma

PNET = Primitive neuroectodermal *tumor*
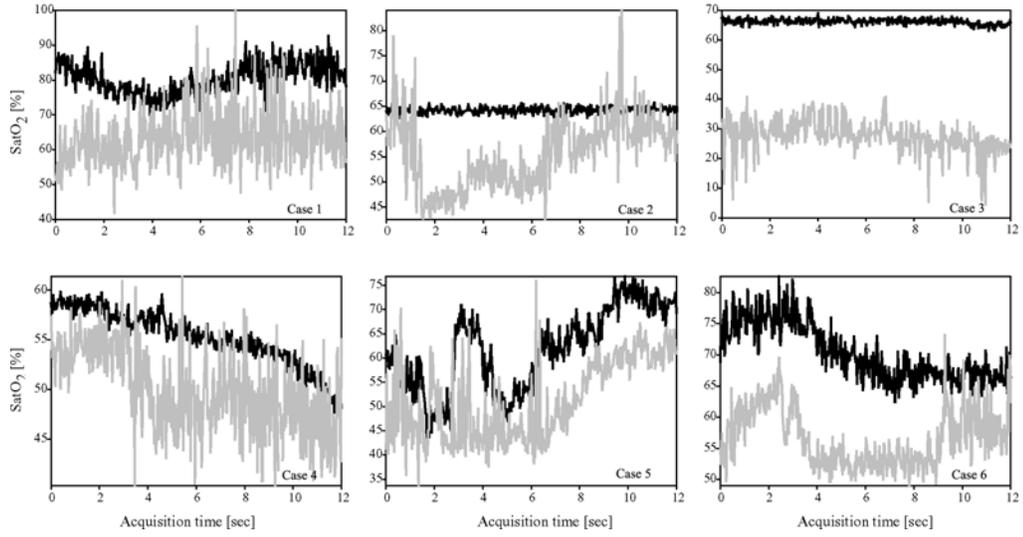
Figure 3-9. Representative time histories of the estimated *SatO₂* levels of normal cortex (black) and tumor (grey) from all six patients.

3.7. Discussion and conclusion

In this study, a new Hb oxygenation extraction algorithm was proposed and validated using simulated diffuse reflectance spectra. The algorithm utilizes the spectral profile characteristics of oxy/deoxy-Hb (i.e., $Z_{j,s,n}^{\varepsilon}$) between 450 nm and 600 nm to track the $SatO_2$ level of Hb, which yields a set of lookup functions $S_{j,s,n}$. Certain counterparts $Z_{j,s,n}^{Rd}$ can be also identified in the log-transformed diffuse reflectance spectrum

$(-\ln[Rd(r,\lambda)])$ and can be used in conjunction with the corresponding $S_{j,s,n}$ to extract

the $SatO_2$ level of Hb from the diffuse reflectance spectrum. Based upon the extensive

evaluation conducted, the ideal lookup functions for the proposed algorithm are $S_{2,6,2}$ for

$SatO_2 \geq 40\%$, and $S_{4,6,3}$ for $SatO_2 < 40\%$. The former lookup function utilizes the location

of the second inflection point in filtered $-\ln[Rd(r,\lambda)]$, $Z_{2,6,2}^{Rd}$, as input; the latter the

fourth local maximal curvature, $Z_{4,6,3}^{Rd}$. When the source-detect separation is less than 0.3

cm, the algorithm is highly accurate for a wide range of optical properties of the

measured target.

Despite being a statistical model, MC simulation for photon migration has

become the gold standard for predicting photon migration in biological tissues [58]. One

critical advantage of the MC model is that it can be used to evaluate a broad range of

tissue optical characteristics efficiently. While constructing the $Rd_{sim}(r,\lambda)$ database for

the algorithm validation, the ranges of the optical properties selected encompass the

majority of *in vivo* biomedical tissues. The outcome of the validation shows that the

algorithm provides satisfactory accuracy, in terms of estimating Hb oxygenation, relative

to pulse oximetry [60]. Furthermore, the estimation performance of the algorithm is fairly

constant over the entire optical property range, as indicated by low and steady estimation

errors. This demonstrates the applicability of the algorithm to extract the $SatO_2$ level of

Hb from diffuse reflectance spectra measured for various tissue types *in vivo*.

Through the derivation and validation processes, several advantages of the

proposed algorithm were noticed. The operation of the algorithm involves conducting

two transformations to the input (i.e., $Rd(r,\lambda)$) and applying the target spectral feature

location (i.e., $Z_{j,s,n}^{Rd}$) to its corresponding lookup function $S_{j,s,n}$. This is relatively simple and straight-forward, versus other models that often require a repeated fitting routine for multiple variables. Because of this advantage, the proposed algorithm can be used for real-time $SatO_2$ assessments.

Furthermore, with an appropriate selection of the spectral profile features and hence the lookup functions, the algorithm is insensitive to the scattering properties and BVF of the biological media, as well as to the source-to-detector separation. In other words, the proposed Hb extraction algorithm with a set of established lookup functions can be immediately applied to the *in vivo* diffuse reflectance spectra acquired from various tissue types using optical probes with a wide range of source-detection geometry. The utilization of DWT in the proposed extraction algorithm also reduces the impact of spectral noise on the accuracy of the $SatO_2$ level assessment. As mentioned before, the DWT process is equivalent to signal filtering; unwanted noise in the signal is removed by a tunable linear band-pass filter. In addition, the noise level in signals can be assessed by DWT with a small scale, which provides a convenient way to access the quality of the signals (i.e., *S/N*) instantaneously.

The proposed algorithm uses the spectral profile characteristics in a diffuse reflectance spectrum to determine its corresponding $SatO_2$ level of Hb. Hence, intensity reference measurements employed in many other $SatO_2$ interpretation algorithms are not needed here. However, calibration to the diffuse reflectance spectroscopy system is required to remove all possible spectral profile alterations induced by the instrumentation itself.

29

To ensure the accuracy of the extraction algorithm, the spectral profile characteristics of the input signals (i.e., $Rd(r,\lambda)$) must be well preserved. In other words, the success of applying the algorithm hinges upon the spectral resolution and the *S/N* of the input diffuse reflectance spectra. During the development and evaluation processes, a 2 nm spectral resolution was used in both $\varepsilon^{SatO2}(\lambda)$ and $Rd_{sim}(r,\lambda)$. This spectral resolution is easily achievable with the spectrometers in today's market. Further investigation is required to elucidate the impact of lower spectral resolution on the accuracy of the extraction algorithm. In terms of *S/N*, we believe the *S/N* level of the signal, as defined by (9), should be higher than 700 and 70 for $S_{2,6,2}$ and $S_{4,6,3}$, respectively, in order to achieve acceptable algorithm accuracy. This conclusion is derived based upon the *S/N*-estimation error analysis shown in Figure 3-7.

The clinical relevance of the *SatO2* extraction algorithm also was confirmed through a couple of *in vivo* experiments. In the fingertip ischemia experiment, the *SatO2* level of the fingertip under normal conditions is about 70%. The algorithm immediately reported regional tissue hypoxia once the ischemia was induced and the recovery of *SatO2* level once the occlusion was cleared. These results are similar to the studies published previously [26, 42]. As shown in Figure 3-8, the time histories of the *SatO2* variations derived from the two source-detector separations are very similar, which demonstrates the insensitivity of the algorithm to the source-detector separation. The further reduction in the discrepancy between the two *SatO2* trends in Figure 3-8 during the steady-state ischemic period may be attributed to the disappearance of the normal oxygen gradient across the epidermis under ischemic conditions [61].

The $SatO_2$ level of normal cortex reported here also agrees with a previously reported level [62]. It was noted that, in some cases, the $SatO_2$ level fluctuated significantly during the recording period, as shown in Figure 3-9. These alterations, in our opinion, may have been primarily caused by movement of the surgeon's hand during the data acquisition period. In a previous study, excessive movement along the axial direction was found to sometimes induce large variations in probe contact pressure, thereby altering local hemodynamics [63]. Nevertheless, the $SatO_2$ levels detected from the brain tumor areas were consistently lower than those from normal cortex, which is a well known physiological characteristic of brain tumors [64]. This trend may be used as an additional indicator for *in vivo* brain tumor demarcation using optical spectroscopy.

The extraction algorithm operates within the spectral region, 450 nm to 600 nm, where the Hb absorption spectrum is rich in spectral profile features. Unfortunately, this is also the region where the Hb absorption is very strong. This characteristic impedes the photons from penetrating deeply into tissue. According to the results generated using the MC simulations, the penetration depth of light within this region usually falls within one or two millimeters, depending on the tissue type and the Hb concentration in the tissue. In addition, the high absorption characteristics of Hb in this spectral region also limits the source-detector separation to preserve the S/N of the signals. These two factors, together, limit the volume of tissue investigated by the diffuse reflectance spectroscopy system employing the extraction algorithm for $SatO_2$ assessment. Under this circumstance, the suitable instrumentation partners for the algorithm would be systems with fiber-optic based setups that acquire diffuse reflectance from tissues using surface probes, catheters

31

or needles. Such a combination will be ideal for studies of *in vivo* microcirculation for which focal information is required.

3.8. Appendix

The continuous wavelet transformation of $\varepsilon^{SatO2}(\lambda)$ is defined by

$$W_s \varepsilon^{SatO2}(u) = \int_{-\infty}^{+\infty} \varepsilon^{SatO2}(\lambda) \cdot \frac{1}{\sqrt{s}} \psi\left(\frac{\lambda - u}{s}\right) d\lambda, \quad (3.10)$$

where $\psi(\lambda)$ is the mother wavelet and s is the scaling parameter and u is the translation parameter. (A1) can be rewritten into a convolution format as

$$W_s \varepsilon^{SatO2}(u) = f \times \psi_s(u), \quad (3.11)$$

where $\psi_s(\lambda) = 1/\sqrt{s} \cdot \psi(-\lambda/s)$ and $\times$ denotes convolution. The wavelet needs to have a zero average $\int_{-\infty}^{\infty} \psi(\lambda) d\lambda = 0$ and the Fourier transform of $\psi_s(\lambda)$ is $\hat{\psi}_s(\omega) = \sqrt{s}\hat{\psi}(s\omega)$. This indicates that the wavelet transform processes the input single in a fashion similar to a tunable band-pass filter [65].

If the wavelet function has n vanishing moments and it can be rewritten as nth derivative of a function [65]. That is $\psi(\lambda) = (-1)^n \cdot d^n \rho(\lambda)/d\lambda^n$. The wavelet transformation can be rewritten into a format of differential wavelet transform defined as

$$W_s^n \varepsilon^{SatO_2}(u) = s^n \frac{d^n}{du^n}(\varepsilon^{SatO_2} \times \rho_s)(u), \quad (3.12)$$

where $\rho_s(\lambda) = 1/\sqrt{s} \cdot \rho(\lambda/s)$. In this application, a Gaussian smoothing function is chosen for $\rho(\lambda)$.

4. Estimation of regional hemoglobin concentration in biological tissues using diffuse reflectance spectroscopy with a novel spectral interpretation algorithm

4.1. Introduction

Abnormal variations in regional hemoglobin (Hb) concentration reflect unusual physiological conditions, such as local ischemia, in the microcirculation of biological tissues. This information provides great insights into various medical conditions and, hence, is highly sought, both in medical research and clinical practice [44, 46, 66]. In the search for non-invasive, *in vivo* and real-time estimates of regional Hb concentration ([Hb]), diffuse reflectance spectroscopy has been proven to be an effective and favorable methodology [67-70] because of its non-invasive, non-destructive nature. When considering retrieving [Hb] information from diffuse reflectance spectra, the most popular approach is to monitor the diffuse reflectance intensities at isosbestic wavelengths, where oxy-Hb and deoxy-Hb have the same absorption properties. The intensities measured at these isosbestic wavelengths are independent of the oxygen saturation ($SatO_2$) level in Hb; however, the intensities still are influenced by the scattering properties of the investigated subject, by excitation intensity, and by collection efficiency. These variables make estimating absolute [Hb] solely based upon diffuse reflectance intensities at isosbestic wavelengths difficult, if not impossible. With more advanced methods, the diffuse theory [46, 53, 67, 71], the Monte Carlo (MC) based inverse model [54], or the empirical model [29, 55, 72] are employed in the process of

retrieving [Hb] information from the diffuse reflectance spectra within a certain spectral wavelength range. Specifically, these methods use a systematic approach to identify the optimal scattering and absorption coefficients that would produce a theoretically-predicted diffuse reflectance spectrum that closely matches the experimental one. From the optimal absorption coefficients, [Hb] information is subsequently derived. However, these methods require a series of rigorous intensity calibrations against tissue phantoms or references to achieve estimate accuracy.

In this paper, we present a new algorithm that aims to retrieve [Hb] from diffuse reflectance spectra measured from *in vivo* tissue using a fiber-optic spectroscopy system. While derivative of diffuse reflectance spectra has been used to reduce the scattering effects [73, 74], the proposed algorithm utilizes the natural logarithmic operation as well as the differential wavelet transform (DWT), which employs the concept of a multi-scale differential operator [75, 76], to effectively quench the scattering effects and remove the excitation intensity effect on diffuse reflectance spectra. The algorithm then employs the idea of isosbestic wavelength to reduce the impact of *SatO₂* variations and estimate absolute [Hb]. The versatility as well as the accuracy of the algorithm was validated and evaluated theoretically and experimentally.

4.2. Methods

The absorption coefficient spectrum, $\mu_a(\lambda)$, of Hb between 500 nm and 600 nm comprises several noticeable valleys and peaks, rendering it very feature-rich relative to the corresponding scattering coefficient spectrum, $\mu_s(\lambda)$. The [Hb] estimation algorithm

presented here was established based upon this attribute, and the detailed derivation processes of the algorithm are provided as follows.

4.2.1. *Photon migration theory*

Photon migration theory describes that the energy of a photon package is reduced by a series of absorption events during the migration process. A package of diffuse reflected photons can be formulated as:

$$E(r,\lambda) = E_0 e^{-\mu_a(\lambda)\cdot l(r,\lambda)} \text{ (J)}, \quad (4.1)$$

where E_0 is the initial energy of the photon package (J), where λ is wavelength (nm), r is the exit location (μm), $E(r,\lambda)$ is the exit energy of the photon package (J) when it remerges at r, $\mu_a(\lambda)$ is the absorption coefficient of the medium (1/cm), and $l(r,\lambda)$ is the migration pathlength of the photon package (cm). It should be noted that $l(r,\lambda)$ is a function of the reduced scattering properties of the medium $\mu_s'(\lambda)$ (1/cm) and r. The summation of the all exit photon packages at a given surface location per unit time forms a steady-state diffuse reflectance spectrum, $Rd(r,\lambda)$ (W), which can be described as:

$$Rd(r,\lambda) = \frac{\sum_{i=1}^{x} E_i(r,\lambda)}{T} = \frac{E_0}{T} \sum_{i=1}^{x} e^{-\mu_a(\lambda)\cdot l_i(r,\lambda)} \approx \frac{E_0}{T} e^{-\mu_a(\lambda)\cdot k(r,\lambda)} \text{ (W)}, \quad (4.2)$$

where x is the number of diffusely reflected photon packages remerged at r and is a probability determined by $\mu_s'(\lambda)$ (1/cm) and r, T is the time to deliver the entire incident photon packages, $k(r,\lambda)$ is a constant calculated from $k(r,\lambda) = -\ln(\sum_{i=1}^{x} e^{-\mu_a(\lambda)\cdot l(r,\lambda)})/\mu_a(\lambda)$. A natural logarithmic operation is applied to

$Rd(r, \lambda)$ for obtaining the absorption characteristics (i.e., $\mu_a(\lambda)$) and the scattering characteristics (i.e., $k(r, \lambda)$). That is:

$$-\ln[Rd(r, \lambda)] = \mu_a(\lambda) \cdot k(r, \lambda) - \frac{E_0}{T} \ (W). \qquad (4.3)$$

As mentioned previously, within a spectral region of 500 to 600 nm, $\mu_s'(\lambda)$ is much smoother than $\mu_a(\lambda)$ in terms of the spectral profile. According Eq. (4.3), $-\ln[Rd(r, \lambda)]$ would have a greater spectral-profile similarity to $\mu_a(\lambda)$ than $Rd(r, \lambda)$.

4.2.2. Differential wavelet transformation

In order to facilitate the extraction of the absorption characteristics of Hb from $-\ln[Rd(r, \lambda)]$, DWT was employed in the algorithm. A wavelet function ψ with n vanishing moments can be rewritten as the nth order derivative of a function $\rho(\lambda)$ [75, 77]. That is:

$$\psi(\lambda) = (-1)^n \frac{d^n \rho(\lambda)}{d\lambda^n}, \qquad (4.4)$$

where the smoothing function, $\rho(\lambda)$, is a Gaussian function in this application. The wavelet function can be dilated using a scale parameter s. That is

$$\psi_s(\lambda) = (-1)^n \frac{d^n \rho_s(\lambda)}{d\lambda^n}, \qquad (4.5)$$

where $\rho_s(\lambda) = 1/\sqrt{s} \cdot \rho(\lambda/s)$. Such manipulations turn a wavelet function into a multiscale differential operator. DWT of a measured spectrum $f(\lambda)$ is defined as

$$W_s^n f(u) = \int_{-\infty}^{+\infty} f(\lambda) \cdot \psi_s(\lambda - u) d\lambda, \qquad (4.6)$$

where u is a translation parameter. Since ψ_s processes a zero average $\int_{-\infty}^{\infty} \psi_s(\lambda)d\lambda = 0$

and the Fourier transform of $\psi_s(\lambda)$ is $\hat{\psi}_s(\omega) = \sqrt{s}\hat{\psi}(s\omega)$, the DWT process is equivalent

to filtering with a tunable band-pass filter [75]. In other word, the unwanted spectral

variations in $f(\lambda)$ are eliminated during the DWT process. In the algorithm, DWT is

applied to $-\ln[Rd(r,\lambda)]$, denoted by $W_s^n\{-\ln[Rd(r,u)]\}$. Based on the explanation of the

spectral characteristics of Eq. (4.3) in the previous section, the application of DWT in the

algorithm is expected to suppress the effect of $\mu_s^{'}(\lambda)$ in $k(r,\lambda)$ and removes E_0/T in

Eq. (4.3). This allows the algorithm to isolate the contributions of $\mu_a(\lambda)$ to $-\ln[Rd(r,\lambda)]$.

4.2.3. DWT isosbestic wavelengths

As mentioned in the Introduction section, several isosbestic wavelengths can be found in

the absorption spectra of oxy and deoxy hemoglobin. The same phenomenon also can be

found in the transformed spectrum, $W_s^n\{-\ln[Rd(r,u)]\}$; they are referred as DWT

isosbestic wavelengths (DIW) in this paper. The algorithm was assumed that the intensity

of $W_s^n\{-\ln[Rd(r,u)]\}$ at a given DIW located at $u = h$ (nm), is not only insensitive to the

scattering effects but also unaffected by $SatO_2$ variations. As a result, $W_s^n\{-\ln[Rd(r,h)]\}$

could be a good indicator for [Hb] estimation. To simplify the notation,

$W_s^n\{-\ln[Rd(r,h)]\}$ is replaced by $W_r(n,s,h)$ in the following discussion. Because there

could be multiple potential $W_r(n,s,h)$s for [Hb] estimation, a thorough search was carried

out with all combinations of $n = 1$ to 3 and $s = 2$ to 8 to identify all possible $W_r(n,s,h)$s in

their corresponding $W_s^n\{-\ln[Rd(r,u)]\}$. The performance of each $W_r(n,s,h)$ is later evaluated in section 4.2.5

4.2.4. Monte Carlo simulation

In order to investigate the relationship between $W_r(n,s,h)$ and [Hb] under various scattering and hemodynamic conditions, a Monte Carlo (MC) simulation model of photon migration was used to create a comprehensive diffuse reflectance spectrum database ($Rd_{sim}(r,\lambda)$). In the simulations, a semi-infinite medium with homogenous optical properties was used to mimic biological tissues. During each simulation, a total of three million photons was injected into the medium at the origin of a cylindrical coordinate (i.e., $(r,z) = (0,0)$). The diffuse reflectance signals were produced by recording the energy of the reflected photons according to the exit location r on the surface.

In the simulations, Hb was considered to be the only chromophore, because of its dominating absorption nature between 500 nm and 600 nm in biological tissues. The absorption property of the medium in the simulations, therefore, was defined by the following equation:

$$\mu_a(\lambda) = [Hb] \times [SatO_2 \times \varepsilon^{oxy}(\lambda) + (1 - SatO_2) \times \varepsilon^{deoxy}(\lambda)] \ (1/cm), \qquad (4.7)$$

where [Hb] is the Hb concentration (g/dL), $SatO_2$ is the hemoglobin oxygen saturation level (%), $\varepsilon^{oxy}(\lambda)$ is the extinction coefficient for oxygenated Hb (dL/g/cm), and $\varepsilon^{deoxy}(\lambda)$ is the extinction coefficient for deoxygenated Hb (dL/g/cm). The reduced scattering coefficients in biological tissues were approximated by the following formula [53, 57]:

$$\mu_s^{'}(\lambda) = A \times w^{-B} \ (1/\text{cm}), \qquad (4.8)$$

where $w = \lambda \times 10^3$.

The ranges of all variables used to generate $Rd_{sim}(r,\lambda)$ are provided in Table 4-1. They were selected to encompass the major types of biological tissue, under all possible hemodynamic conditions [58]. The variable r measures photon exit distance from the source and its extent can cover the source-detection separations commonly used in the *in vivo* diffuse reflectance studies.

Table 4-1. Variables used to construct $Rd_{sim}(r,\lambda)$ and the ranges used

Variable	Start Value	Increment	End Value
r	75 (μm)	50 (μm)	9975 (μm)
[Hb]	0.075 (g/dL)	0.075 (g/dL)	1.200 (g/dL)
$SatO_2$	20 (%)	20 (%)	100 (%)
A	600	100	1400
B	0.9	0.1	1.5
λ	400 (nm)	2 (nm)	650 (nm)

4.2.5. Optimal $W_r(n,s,h)$ identification

The $W_r(n,s,h)$s identified in Section 4.2.3 were further evaluated in accordance with their stability against scattering and $SatO_2$ variations to identify the ideal $W_r(n,s,h)$ for the proposed algorithm. The evaluation was performed with $Rd_{sim}(r,\lambda)$ exclusively. The variability of each $W_r(n,s,h)$, within the ranges of scattering and $SatO_2$ defined in Table 4-1, was quantitatively assessed for each r and [Hb] combination. In other words, the mean value and the standard deviation of $W_r(n,s,h)$ derived from $Rd_{sim}(r,\lambda)$ sharing with the same r and [Hb] were calculated. Please note that, according to Table 4-1, [Hb] and r are discrete arithmetic sequences, and they are (0.075, 0.150,…, 1.20) and (75, 125,…,2975),

respectively. The calculated mean value was denoted by $M_{r,[Hb]}(n,s,h)$ and the standard deviation was denoted by $S_{r,[Hb]}(n,s,h)$. The average relative standard deviation (RSD) of each $W_r(n,s,h)$ is defined using the following equation:

$$\sum_{r=75}^{2975}\left\{ \left. \sum_{[Hb]=0.075}^{1.2} \frac{S_{r,[Hb]}(n,s,h)}{D_{r,[Hb]}(n,s,h)} \middle/ 16 \right\} \middle/ 59 \right. \text{ (\%)}, \quad (4.9)$$

where

$$D_{r,[Hb]}(n,s,h) = \left\{ \left| M_{r,[Hb]-0.075}(n,s,h) - M_{r,[Hb]}(n,s,h) \right| + \left| M_{r,[Hb]+0.075}(n,s,h) - M_{r,[Hb]}(n,s,h) \right| \right\}/2$$
for $0.075 < [Hb] < 1.2$,

$$D_{r,[Hb]}(n,s,h) = \left| M_{r,[Hb]+0.075}(n,s,h) - M_{r,[Hb]}(n,s,h) \right| \text{ for [Hb]=0.075, and}$$

$$D_{r,[Hb]}(n,s,h) = \left| M_{r,[Hb]-20}(n,s,h) - M_{r,[Hb]}(n,s,h) \right| \text{ for [Hb]= 1.2.}$$

The ideal $W_r(n,s,h)$ for the proposed [Hb] estimation algorithm was considered to be one that produces the lowest average RSD value.

4.2.6. *Tissue phantom preparation*

In order to evaluate the proposed algorithm, a series of experiments were carried out using liquid tissue phantoms. These phantoms were constructed by mixing a saline solution with whole blood and scatterers, which mimic the absorption and scattering properties, respectively, of biological tissues. The blood samples were collected from healthy human subjects, following a procedure approved by the Institutional Review Board of Florida International University. Once collected, the samples were heparinized using heparin at a concentration of 55 USP/mL. The [Hb] of each phantom was determined by the volume of the whole blood added, and the [Hb] of the whole blood sample measured by means of a complete blood count exam. The scattering properties of

the phantom were controlled by the concentrations of 1-μm diameter polystyrene microspheres ([Mpoly]) (Polybead Microspheres 1.00 μm, Polysciences Inc., Warrington PA) with a refractive index of 1.59. The resulting scattering effect from the microsphere was estimated using a Mie Theory calculator [78]. During the experiment, the tissue phantom was agitated constantly, using a magnetic stir bar to prevent the precipitation of red blood cells and microspheres.

Two sets of tissue phantom experiments were employed to further evaluate the utility of the proposed algorithm. The first set of experiments was designed to verify that $W_r(1,6,516.5)$, identified theoretically using $Rd_{sim}(r,\lambda)$, is insensitive to $SatO_2$ variations. Two tissue phantoms (Phantoms 1 and 2) were oxygenated by means of oxygen bubbling, to elevate the $SatO_2$ level to 100%. Sequentially, the phantoms were deoxygenated by means of nitrogen bubbling at a flow rate of 0.1 L/min. The temperature of the tissue phantoms was kept at 37 to 38 degrees Celsius. The diffuse reflectance spectra were acquired every 5 minutes during the deoxygenation process. The scattering properties from the microsphere of Phantoms 1 and 2 were those described in Group 4 of Figure 4-1. The [Hb] contents of the two phantoms were 0.301 g/dL and 0.152 g/dL, respectively.

In the second set of experiments, 44 liquid tissue phantoms were prepared with various combinations of [Hb] and [Mpoly] to evaluate the effects of scattering variation upon $W_r(1,6,516.5)$. The 44 liquid tissue phantoms were divided into 4 groups, according to the range of [Mpoly], and their corresponding scattering properties from the microsphere are shown in Figure 4-1. Each group contained 11 phantoms and their [Hb] were 0.077, 0.152, 0.227, 0.301, 0.375, 0.448, 0.520, 0.591, 0.732, 0.870, and 1.006 g/dL.
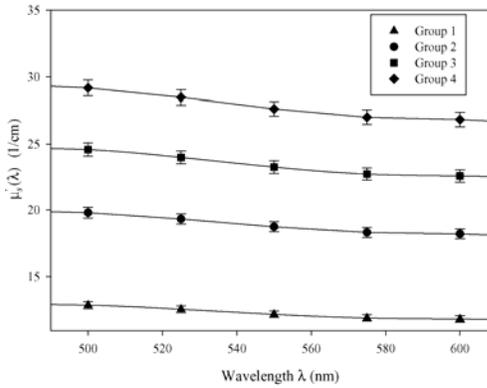
Figure 4-1. The reduced scattering coefficients of all tissue phantom groups, contributed by the microspheres. The solid lines are the mean values (n=11) and the error bars are standard deviations. Please note that variations in $\mu_s'(\lambda)$ were a result of diluting the tissue phantoms (i.e., [Mpoly]) after adding whole blood.

4.2.7. *In vivo clinical study*

In order to demonstrate the clinical application of the proposed algorithm, the algorithm was applied to *in vivo* diffuse reflectance spectra collected from human brain tissue. Six pediatric patients who were undergoing a craniotomy at Miami Children's Hospital for brain tumor resection participated in the study. Diffuse reflectance spectra were acquired using a fiber-optic spectroscopy system which will be introduced in the next section. The surgeon placed the probe in direct contact with the brain tissue, and diffuse reflectance spectra were collected from regions of normal cortex and tumor in each patient. The normal cortex region was an area distant from the resection zone and the tumor region was confirmed by histological examination of the biopsy samples. Consent was obtained from patients and their parents prior to the experiment. The protocol of this clinical study was approved by the Western Institutional Review Board and the Institutional Review Board of Florida International University. Additional details regarding the methodology of this clinical study can be found in reference [59].

4.2.8. Optical instrumentation

To acquire diffuse reflectance spectra from the liquid tissue phantoms, a multi-spectrometer system was used. The system consisted of a tungsten-halogen light (LS-1, Ocean Optics, Dunedin, FL, USA) and three spectrometers (USB 2000, Ocean Optics, Dunedin, FL, USA) to record diffuse reflectance signals. For excitation light delivery and reflected light collection, a custom-made fiber-optic probe was used. The probe contained three fibers for reflected light collection and one for excitation light delivery. The outer and core diameters of each fiber were 236 μm and 200 μm, respectively. The arrangement of the excitation and collection fibers in the probe is depicted in Figure 4-2. Each collection fiber was connected to a designated spectrometer; therefore, diffuse reflectance spectra were measured from the phantom samples at three different r values. The measured diffuse reflectance spectra were calibrated against a reflectance standard (FGS-20-02c, Avian Technologies, NH, USA) to remove all spectral alterations induced by the instruments.
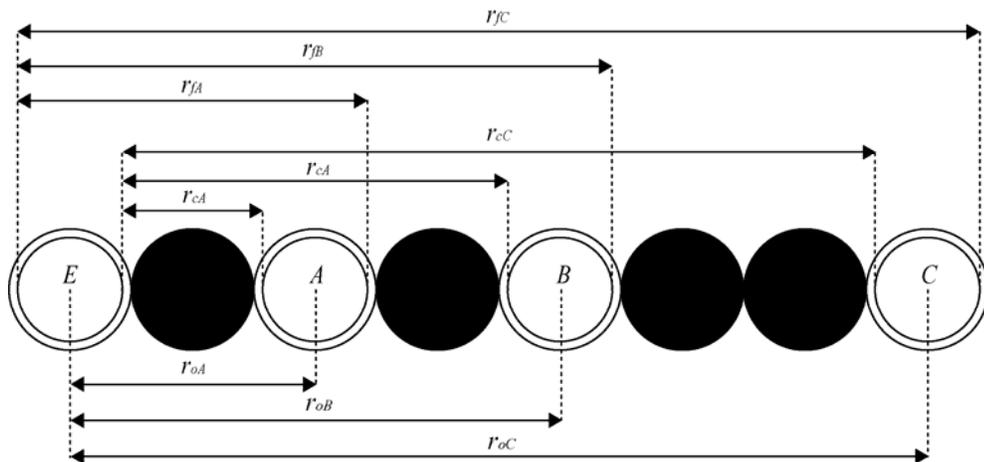
Figure 4-2. A schematic of the optical probe. The black circles represent the spacers and the white circles represent the optical fibers. The letter *E* indicates the excitation fiber; the letters *A*, *B*, and *C* identify the detection fibers. The inner

circles of the optical fibers represent their cores. The distances between the center of the excitation fiber and those of the three detection fibers are r_{oA}=472 µm, r_{oB}=944 µm, and r_{oC}=1652µm. The shortest distances between the excitation fiber and the three detection fibers are r_{cA}=372 µm, r_{cB}=844 µm, and r_{cC}=1552 µm; and the longest distances r_{fA}=572 µm, r_{fB}=1044 µm, and r_{fC}=1752 µm.

For *in vivo* spectral data acquisition during the brain tumor study, the fiber-optic spectroscopy system used here comprised the same excitation light source and calibration procedure, but only one spectrometer. The optical probe for this clinical study comprised seven 300 µm optical fibers, one of which was connected to the light source for excitation, one unused, and the remaining five connected to the spectrometer for detection. The average source-detector separation of this probe is about 460 µm. During the experiment, diffuse reflectance spectra were recorded at a rate of 33 Hz for 12 seconds at each investigated site.

4.2.9. Signal to noise ratio monitoring

During the validation and evaluation process, it was felt that the noise levels in the simulated and experimentally-acquired diffuse reflectance spectra might influence the performance of the algorithm. Therefore, the signal to noise ratio (*S/N*) of all spectra were calculated. The scale parameter s in DWT provided a convenient means by which to investigate the signal level of a diffuse reflectance spectrum at various frequencies. By setting *s*=1 in DWT, DWT isolates the highest frequency component of the signal, which was considered the noise in the spectrum. According to the *s* and *n* parameters used in $W_s^n\{-\ln[Rd(r,h)]\}$, the S/N of $-\ln[Rd(r,\lambda)]$ can be estimated using Eq. (4.10).

$$S/N(s,n) = \frac{\left| \sum_{u=500}^{560} W_s^n \{-\ln[Rd(r,u)]\} \right|^2}{\left| \sum_{u=500}^{560} W_1^n \{-\ln[Rd(r,u)]\} \right|^2} \qquad (4.10).$$

4.3. Results

4.3.1. Monte Carlo simulation

Figure 4-3 presents a set of sample spectra for the purpose of demonstrating how the proposed spectral manipulation process in the algorithm suppresses the variations induced by scattering properties and $SatO_2$ in diffuse reflectance spectra. Figure 4-3 (a) plots 24 diffuse reflectance spectra selected from the $Rd_{sim}(r,\lambda)$ database. While the r and [Hb] values of these spectra are constant, their corresponding combinations of $SatO_2$ level and reduced scattering coefficient varied significantly. Clearly, discrepancies in the intensity as well as the profile of these spectra demonstrate the strong influences of scattering properties and $SatO_2$ on diffuse reflectance spectra. The diffuse reflectance intensities at isosbestic wavelengths, like 538 nm, are not constant within this spectral set, despite the constant level of [Hb]. Based upon the transformed spectra $W_s^n \{-\ln[Rd(r,u)]\}$ illustrated in Figure 4-3 (b), it is observed that the effects of both scattering properties and $SatO_2$ on the intensities of $W_s^n \{-\ln[Rd(r,u)]\}$ at several wavelengths are greatly reduced. These wavelengths are identified as DIWs, and the intensities of $W_s^n \{-\ln[Rd(r,u)]\}$ at these wavelengths are represented by $W_r(n,s,h)$ in the algorithm. As shown in Figure 4-3 (b), within the spectral region of interest, four

different $W_r(n,s,h)$ are found in the $W_s^n\{-\ln[Rd(r,u)]\}$ using the $s=6$ and $n=1$ combination. A total of 89 $W_r(n,s,h)$ were identified using the combinations of $n = 1$ to 3 and $s = 2$ to 8.
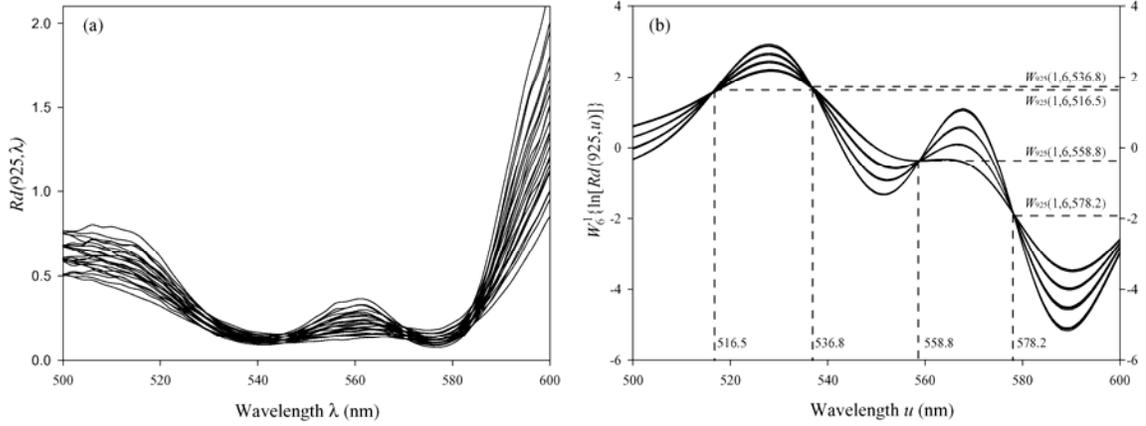
Figure 4-3. (A) 24 diffuse reflectance spectra from the MC simulation database. These spectra were generated using $r = 925$ μm, [Hb]=0.75 g/dL, and all possible combinations of B= [0.9, 1.1], A=[600, 700, 800], and $SatO_2 = $ [40%, 60%, 80%, 100%]. (B) The corresponding transformed diffuse reflectance spectra, $W_{s=6}^{n=1}\{-\ln[Rd(925,u)]\}$. The dashed lines indicate the locations of the DIWs (h (nm)) and their corresponding intensities $W_{r=925}(n=1,s=6,h)$, where h= 516.5, 536.8, 558.8, and 578.2 nm .

Since the MC simulation model is a probability-based method and only a finite number of photons was used in each run of simulation, statistical noise does exist in each $Rd_{sim}(r,\lambda)$. The S/N of $Rd_{sim}(r,\lambda)$ would drop significantly when r becomes exceedingly large. Moreover, the intensity of $Rd_{sim}(r,\lambda)$ may be reduced to zero at one or more wavelengths, when r is large. This would fail the logarithmic operation proposed in the spectral condition procedure of the algorithm (i.e., Eq. (4.3)). To avoid these unwanted effects in the $W_r(n,s,h)$ evaluation process, the simulated spectra containing zero intensity was identified and eliminated at each r, and the average S/N of transformed spectra was estimated and recorded using Eq. (4.10). The results of the $Rd_{sim}(r,\lambda)$ survey

indicate that the average *S/N* declines and the number of unusable spectra ascends sharply when *r* is greater than 3000 μm, as shown in Figure 4-4. Based upon this observation, the evaluation for $W_r(n,s,h)$ was conducted using $Rd_{sim}(r,\lambda)$ with $r < 3000$ μm. This exclusion reduces $Rd_{sim}(r,\lambda)$ to a total of 297360 spectra; 18585 spectra per [Hb] level and 5040 per *r* value.
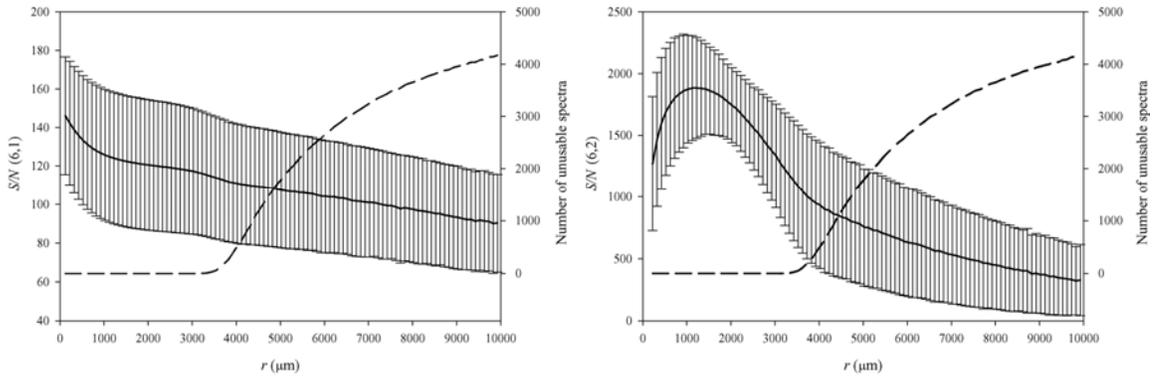
Figure 4-4. The signal qualities of the diffuse reflectance spectra produced by the MC simulation as a function of *r* for two representative *s-n* combinations. The solid lines represent the mean *S/N* of the transform spectra and the error bars are standard deviations. The long dashed lines represent the number of unusable spectra.

Through the evaluation of $W_r(n,s,h)$, it was found that $W_r(1,6,516.5)$ produces the lowest average RSD value, 22.75%. Furthermore, the plot of $W_r(1,6,516.5)$ versus [Hb], shown in Figure 4-5, ascertains its applicability in [Hb] estimation, as it has a relatively small deviation at each [Hb] despite large variations in scattering and $SatO_2$. Figure 4-5 also shows that the relationships between $W_r(1,6,516.5)$ and [Hb] can be approximated by a set of polynomial functions ($R^2 > 0.9$), which become the prediction functions of $W_r(1,6,516.5)$ in the [Hb] estimation algorithm.

The effects of r on the prediction functions also were evaluated according to the probe geometry depicted in Figure 4-2. Specifically, the prediction functions for the shortest, the longest, and the central ranges of r (i.e., r_c, r_f, and r_o, respectively) of each collection fiber were calculated and compared. The results of this investigation, as shown in Figure 4-5, suggest that the prediction function alters when r is changed. For each collection fiber, the separation between the prediction functions of r_c and r_f, increases when [Hb] increases. This phenomenon is especially prominent when the detection fiber is moved closer to the excitation fiber, due to the fact that the overall slope of the prediction function increases when r decreases.
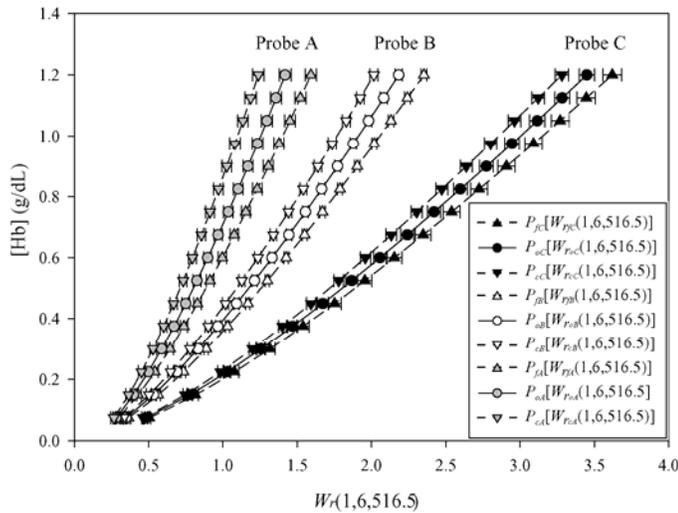
Figure 4-5. The relationships between [Hb] and W_r(1,6,516.5) at various r values derived from the reduced $Rd_{sim}(r,\lambda)$ set produced by the MC simulation model. The values of r were determined according to the probe geometry shown in Figure 4-2. The error bars are the standard deviations incurred by the variation of scattering coefficients and $SatO_2$ levels. The lines are the polynomial functions (P) fitted to the relationship between W_r(1,6,516.5) and [Hb].

4.3.2. Tissue phantom experiments

In the first set of tissue phantom experiments, two tissue phantoms (Phantoms 1 and 2) were used. $W_{rA}(1,6,516.5)$, $W_{rB}(1,6,516.5)$ and $W_{rC}(1,6,516.5)$ then were calculated using the diffuse reflectance spectra acquired from the phantoms through the collection fibers A, B and C, respectively, at various time points during the deoxygenation process. The outcomes of this set of experiments, as presented in Figure 4-6, demonstrate that $W_r(1,6,516.5)$ remains stable during the deoxygenation process. This trend supports $W_r(1,6,516.5)$ being insensitive to variations in $SatO_2$.
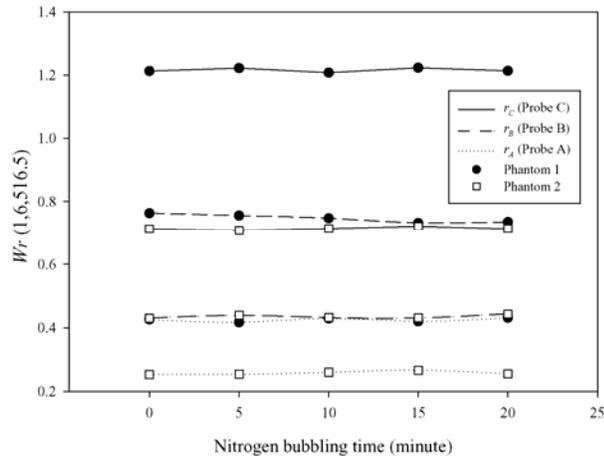
Figure 4-6. $W_r(1,6,516.5)$versus $SatO_2$ levels in the tissue phantoms. The closed circles and open squares represent the mean values of $W_r(1,6,516.5)$, calculated from the diffuse reflectance spectra acquired from the tissue phantoms during the deoxygenation process. Repeat measurements were taken for each data point (n=5), but the error bars for these measurements are too small to show.

In the second set of tissue phantom experiments, 44 phantoms with various scattering properties and [Hb] levels, as defined in Section 2.6, were used. The results of this evaluation are shown in Figure 4-7, where all 44 $W_{rA}(1,6,516.5)$s, $W_{rB}(1,6,516.5)$s, and $W_{rC}(1,6,516.5)$s are displayed as a function of [Hb]. These results confirm that the

central prediction function of the three collection fibers (i.e., P_{oA}, P_{oB} and P_{oC}) depicted in

Figure 4-4 also match nicely with $W_r(1,6,516.5)$s derived from the experiments. The

deviation between the experimental data points and the prediction function is most

prominent in the data from fiber *A*, where the average source-detector separation is the

shortest. This phenomenon is comparable to the results derived from the simulated

diffuse reflectance spectra shown in Figure 4-5. However, the prediction function P_{oC}

fails to extrapolate the actual hemoglobin content when [Hb] increases above 0.6 g/dL.

The estimated [Hb] of the tissue phantoms was obtained by applying $W_{rA}(1,6,516.5)$s,

$W_{rB}(1,6,516.5)$s, and $W_{rC}(1,6,516.5)$s to their corresponding prediction functions (P_{oA}, P_{oB}

and P_{oC}). The average relative estimation errors (i.e., |actual [Hb] - estimated [Hb]|/actual

[Hb]) of the prediction functions were 17.57%, 9.84% and 6.86% for fibers *A*, *B* and *C*,

respectively.
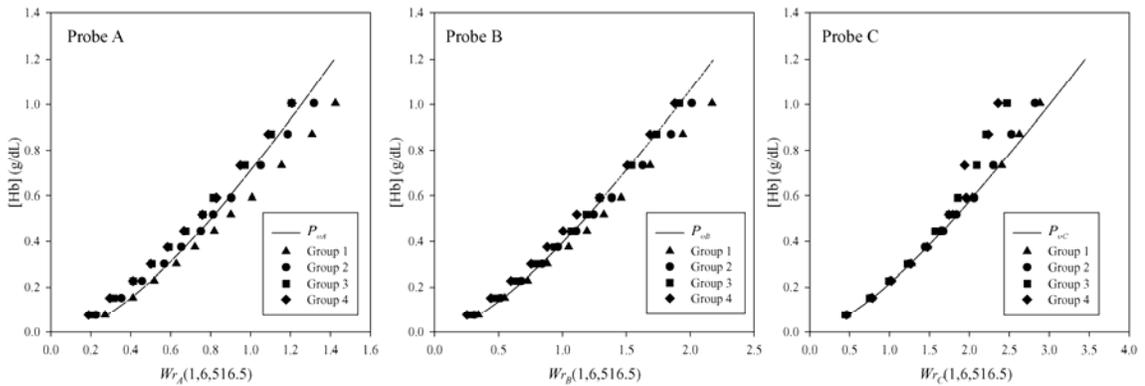
**Figure 4-7. The relationship between $W_r(1,6,516.5)$ and the actual [Hb] of the tissue
phantoms. The different symbols are the average $W_{rA}(1,6,516.5)$, $W_{rB}(1,6,516.5)$ and
$W_{rC}(1,6,516.5)$ (n=5) calculated by the algorithm, using the diffuse reflectance
spectra acquired from different scattering groups of the tissue phantoms. The solid
lines are the central predication function of each fiber (i.e., P_{oA}, P_{oB} and P_{oC})
obtained from MC simulation. The goodness-of-fit for the data points using the
corresponding central prediction curve is R^2=0.935 for fiber *A*, R^2=0.964 for fiber *B*,
and R^2=0.920 for fiber *C*.**

The quality of the spectral signals acquired from the tissue phantoms was estimated in accordance with *S/N*(6,1) defined in (10). The results of the calculations, shown in Figure 4-8, suggest that *S/N* remained relatively stable among the diffuse reflectance spectra collected from fibers *A* and *B*, despite the increase in absorption properties. However, due to a greater source-detector separation of fiber *C*, *S/N*(6,1) drops below 110 when [Hb] elevates above 0.6 g/dL. This degradation in signal quality could explain why the central predication function for probe *C* (i.e., P_{oC}) does not fit the experimental data points well when [Hb] is above 0.6 g/dL. If only the tissue phantoms with [Hb] below 0.6 g/dL were considered, the relative estimation errors for fiber *C* using P_{oC} would reduce to 3.27 %.
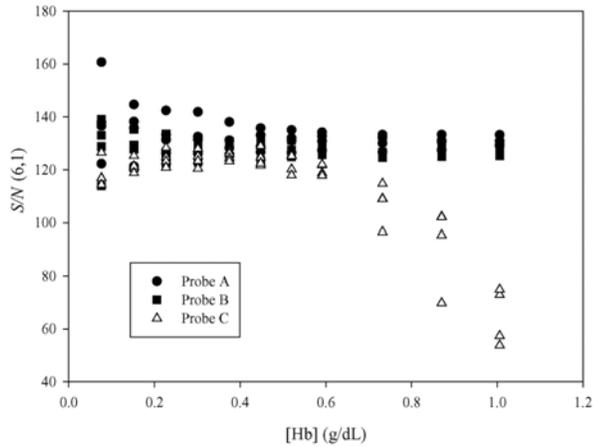
Figure 4-8. *S/N* of the transformed spectra from the tissue phantom evaluation experiments

4.3.3. In vivo clinical experiments

The average source-detector separation distance of the optical probe used in the *in vivo* study is fairly close to r_{oA}; hence, P_{oA} was used as the prediction function to estimate [Hb] within the *in vivo* brain tissues. Table 4-2 provides demographic and histological

information on the six pediatric patients studied. For each investigated area, the average estimated [Hb] and the corresponding standard deviation were calculated from the diffuse reflectance spectra recorded during the entire 12-second acquisition period. The average estimated [Hb] of the normal cortex and the tumor from the study are summarized in Table 4-2. The results indicate that, within each patient, the average [Hb] in tumor is relatively greater than the average [Hb] measured in normal cortex. The overall average [Hb] of the six patients was 0.37 ± 0.18 g/dL in normal cortex and 0.99 ± 0.57 g/dL in tumor tissue. The $S/N(6,1)$ of the diffuse reflectance spectra acquired in this clinical study was 139.32 ± 24.33, which suggests that estimation accuracy was not adversely affected by signal quality.

Table 4-2. Demographic data on the 6 patients who participated in the clinical study

Case #	Gender	Age	Tumor type	Normal cortex [Hb] (g/dL)	Tumor [Hb] (g/dL)
1	M	1	PNET	0.26 ± 0.07	0.40 ± 0.10
2	F	9	PNET	0.59 ± 0.01	1.30 ± 0.64
3	M	10	Pilocytic astrocytoma	0.20 ± 0.01	0.91 ± 0.02
4	F	5	Angioglioma	0.22 ± 0.04	1.00 ± 0.84
5	F	6	Astrocytoma	0.48 ± 0.22	0.85 ± 0.18
6	F	9	Astrocytoma	0.49 ± 0.06	1.52 ± 0.17

PNET = Primitive neuroectodermal tumor

4.4. Discussion and Conclusions

In this section, we present a new algorithm for retrieving absolute [Hb] information from diffuse reflectance spectra acquired from *in vivo* tissue, using a fiber-optic spectroscopy system. The new algorithm employs the natural logarithmic operation and DWT to reduce the effects of scattering in the original diffuse reflectance spectra, and then utilizes DIW in the transformed spectra to remove the effects of $SatO_2$ in Hb. As the result, the

intensity at DIW of the transformed spectra, denoted by $W_r(n,s,h)$, is a good indicator of [Hb] estimation. An extensive set of diffuse reflectance spectra produced by a MC simulation model was used to validate this idea, and it was found that $W_r(1,6,516.5)$ is the optimal indicator for the proposed [Hb] estimation algorithm, because of its insensitivity to variations in scattering properties and $SatO_2$. A r-dependent prediction function was sequentially produced, based upon the relationship between $W_r(1,6,516.5)$ and [Hb]. The accuracy of the derived prediction functions and, hence, the algorithm were further evaluated using a set of tissue phantom studies. The results of these evaluations show that the average estimation error of the prediction functions is about 12 %; and the estimation errors increase as source-detection separation r decreases. Finally, the algorithm was applied to a set of diffuse reflectance spectra obtained from *in vivo* normal and neoplastic areas in brain, which revealed a trend towards higher [Hb] in brain tumors.

Rather than solving an inverse problem using fitting routines, the proposed algorithm uses a forward operation to estimate [Hb]. The algorithm employs two transformations - a logarithmic operation and DWT - to calculate $W_r(1,6,516.5)$ as the input for the prediction function. The main purpose of these transformations is to suppress the effects of scattering properties and $SatO_2$ on [Hb] estimates. The simplicity of the proposed algorithm reduces the computation overhead and makes real-time implementation of the algorithm more feasible. However, it should be noted that the prediction function must be pre-established in accordance with the design of the fiber-optical probe (i.e., the source-detection separation r). Another advantage of the algorithm is that the excitation intensity effect from the light source is removed during the process. Therefore, calibration of the optical systems only needs to remove wavelength-dependent

spectral alterations induced by the instruments. This can be achieved easily by calibrating the instrument against a standard or a calibration light source without using an intensity-dependent reference.

The range of [Hb] used in the validation and evaluation processes of the [Hb] estimation algorithm is considered suitable for biological tissues. For normal human tissues, Wang et al. estimated [Hb] as 0.824 g/dL in small bowel, 0.708 g/dL in large bowel, and 0.790 g/dL in the peritoneum [67]. The [Hb] of skin tissue varies from 0.515 g/dL to 0.165 g/dL [53, 67]. The [Hb] in colon was found to be 0.601 g/dL [46], and was 0.258 g/dL in esophagus [29]. Research also has shown that a 46 % to 137 % increase in [Hb] can be observed in tumor tissue [29, 46, 67]. The experimental evaluations show that the central prediction function, derived from the average source-detection separation of the probe geometry, should provide enough accuracy to distinguish variations in [Hb] within this range.

In our *in vivo* brain study, the average [Hb] of normal pediatric cortex was found to be 0.37 ±1.8 g/dL. Whole blood [Hb] in children is about 13 g/dL [79], and the regional cerebral-to-large vessel hematocrit ratio is 0.69 [80]. Based upon the above information, the calculated average blood volume fraction in normal pediatric cortex using the proposed algorithm is 4.17 ± 0.02 %. Previous investigators have reported that the regional cerebral blood volume of gray matter in adults is 4.80 ± 0.37 % using MR imaging [81], and 5.46 ± 1.40 % by PET scan [82], with a brain tissue density of 1.05 g/mL [83]. The value estimated by the algorithm is comparable, but lower than the results generated using other methodologies. This discrepancy may be attributed to the younger ages of the patients in our study and to the fiber-optics system we used, which only

delves 1 to 2 mm deep into cortex. The estimate from the algorithm indicates that the average [Hb] in tumor regions is about three times the average of [Hb] in normal cortex. This physiological characteristic is commonly found in brain tumors, which generally are highly angiogenic and vascular [84]. These results demonstrate the practicality of the proposed [Hb] estimation algorithm for *in vivo* tissue.

According to our validation and evaluation results using theoretical and experimental diffuse reflectance spectra, the factor r has a major impact upon the prediction function. Therefore, the core diameter and the source-detector separation distance need to be factored into considerations when applying the algorithm. In general, the accuracy of the central prediction function increases when r increases and when the core diameter of the fiber decreases (i.e., the range of r is reduced). Theoretically, the estimation algorithm is at its best when the source-detector separation (r) is large and the core diameter of the optical fiber (d) is small. Caution should be exercised when incorporating these two insights into optical probe design, as they inevitably will affect the quality of the spectral signals. According to our spectral signal quality analysis of the simulated and experimental diffuse reflectance spectra, S/N drops when r increases and/or d decreases, which would reduce the accuracy of the [Hb] estimation algorithm.

The algorithm inspects a narrow spectral region where Hb is highly absorbent. This characteristic restricts source-detector separation as well as the penetration depth to a few millimeters, which leads to a small volume of investigation. Small investigation volume could be advantageous when the target is small and has an arbitrary shape, or focal information is needed. In addition, the probe used for such applications will be

small in diameter and, hence, can fit easily into the needles or catheters used during existing examination procedures.

5. In vivo tissue characterization of myocardial infarcts in rabbit hearts using optical spectroscopy

5.1. Introduction

In 2010, an estimated 785,000 Americans were diagnosed with a new myocardial infarction (MI), and an additional 195,000 had a silent first MI [85]. The development of myocardial ischemic injury evolves over time [9], involving complex remodeling processes [86]. For this reason, being able to accurately estimate the severity and extent of myocardial injury post infarction is paramount, both for clinicians and for researchers striving to improve MI management.

Various *in vivo* imaging modalities have been used to evaluate myocardial injury including, among others, contrast-enhanced magnetic resonance imaging (cMRI), positron emission tomography (PET), and single-photon emission computed tomography (SPECT) [35-39]. Due to the size and cost of these imaging systems, integrating them into intraoperative guidance tools during surgical procedures has been both challenging and expensive.

The rapid development of optical spectroscopy for tissue diagnosis over the past few decades demonstrates the high clinical value of this technique [17]. The basic concept behind this technology is to investigate cellular-level activities in tissues by analyzing the interactions between light and bio-molecules. This methodology has been applied successfully to diagnose pathology in a variety of tissues [18-22]. Further, this modality exhibits a number of advantages over others, in that it is low-risk, non-ionizing,

non-invasive, highly efficient, highly sensitive, real-time, portable, and relatively inexpensive. Several studies have demonstrated the *in vivo* applicability of diffuse reflectance spectroscopy when evaluating cardiac hemodynamics [25, 87-89]. In addition, fluorescence spectroscopy has been shown to be effective analyzing relative changes in metabolic status within tissues. Meanwhile, the intrinsic biological fluorophores (collagen and elastin) are good indicators of tissue fibrosis. Fluorescence spectroscopy's applicability estimating tissue damage has been proven in several studies [30-34].

The aim of this study is to utilize two types of optical spectroscopy - diffuse reflectance spectroscopy and fluorescence spectroscopy - to diagnose MI. In a previous study, we explored the time course of myocardial injury post infarction using a similar system in a rat model [90]. For the current study, a rabbit MI model has been developed to further validate the proposed optical methodology. A more detailed histopathological approach and improved instrumental design were used to investigate the condition of chronic myocardial injury.

5.2. Methods

5.2.1. *Animal model*

To conduct the proposed research project, a rabbit model of MI was first developed and established. The use of rabbits and the study protocol were approved by the Institutional Animal Care and Use Committee at Florida International University (#A3096-1).

The rabbits used in the study were New Zealand white rabbits, purchased from Harlan (Somerville, NJ). All rabbits used in this study were female, weighing roughly

3000 grams each. Each rabbit underwent two stages of surgery over the course of the study. The first-stage surgery was designed to induce MI. The rabbit was anesthetized (induced) with ketamine (15 mg/kg, IM) and medetomidine (0.05 mg/kg, IM). The anesthetized rabbit then was intubated using a 3.0 endotracheal tube, through which a ventilator with an anesthesia unit was connected. The respiratory rate and volume were set at approximately 30 breaths per minute and 10 ml, respectively. These values were adjusted, depending upon the weight and size of the rabbit. General anesthesia was maintained using a 2% to 4% isoflurane-oxygen mixture, administered to the rabbit through the ventilator. A left anterior thoracotomy was performed through the 4th or 5th intercostal space to expose the rabbit's heart. The exposed heart was rotated slightly to identify either bifurcation or trifurcation in coronary vessel distribution [91]. To achieve adequate infarction, the major branch artery in the posterior division was ligated at a 50% level from the apex to the base, using a 5.0 silk suture, if the rabbit's coronary vessels were bifurcated. If trifurcated, the lateral division coronary artery was ligated at a 75% level from the apex to the base [92]. Ischemia was confirmed by cardiac cyanosis as well as ST-segment elevation on electrocardiogram (ECG). Once MI induction was completed, the incision was closed and sutured, layer by layer. Buprenorphine, meloxicam and enrofloxacin were used for post-surgical care.

After recovering from the MI induction procedure for three or four weeks, a second-stage surgery was performed on each rabbit, during which MI development was evaluated using the proposed optical methodologies. The MI rabbit was anesthetized, intubated, ventilated and prepped using the same procedures described above. The heart of the rabbit was exposed via a left anterior thoracotomy. The location of this second

59

incision was either the 5th or 6th intercostal space, so as to avoid the vascular scar tissue caused by the earlier MI induction surgery.

5.2.2. *Optical instrumentation*

The fiber-optic spectroscopy system used in the study was designed to acquire both fluorescence and diffuse reflectance spectra from *in vivo* tissue. The system employed a tungsten-halogen light (LS-1, Ocean Optics, Dunedin, FL, USA) for diffuse reflectance spectroscopy and a 337-nm nitrogen laser (VLS-337, Spectra-Physics, Mountain View, CA, USA) for fluorescence spectroscopy. A mini-USB spectrometer (USB 2000, Ocean Optics, Dunedin, FL, USA) was utilized to record wavelength- dependent characteristics of the reflected light from the tissue surface. The recorded spectra were transferred and stored on a laptop computer. A 380-nm long-pass filter was placed at the entrance of the spectrometer to eliminate the reflected excitation laser light.

An optical fiber bundle was designed and built for excitation light illumination and emission light collection. The optical fiber bundle contained a cluster of four identical fibers, Fibers A to D, as shown in Fig. 5-2. The core diameter of the fibers was 600 ± 10 μm; the numerical aperture was 0.22 ± 0.02. In the bundle, Fiber A was used to deliver laser excitation to the tissue surface, Fiber B to deliver broadband white light; and Fiber C to transport re-emitted light from the tissue surface to the spectrometers. Fiber D was unused in this study. The configuration and arrangement of the fibers at the contact end are depicted in Fig. 2. The distal end of the fiber bundle was encapsulated in a stainless steel tube. A small plastic ball was attached to the distal end of the tube for the purpose of reducing the friction and contact pressure between the probe and heart tissue.

The bundle then was handled by a specially-designed retractable holder with a ball joint and flexible arm, which enabled the probe to move in accordance with heart movements and to achieve a specific contact angle.
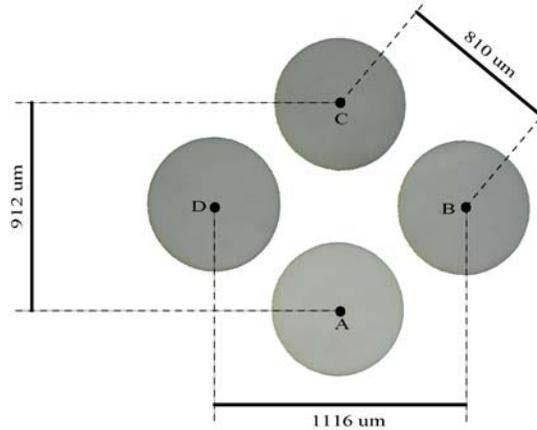
Figure 5-1. Configuration of the optical fiber bundle

5.2.3. Data acquisition

The fiber-optic spectroscopy system described in the previous section was used to acquire spectral data on the exposed heart following the second-stage surgery. During spectral data acquisition, the fiber probe was place on top of the beating heart with constant contact. Measurements were taken from sites that were randomly selected on the surface of the heart, while avoiding the coronary vessels.

To overcome motion artifacts and the physiological variations induced by heart beats during a single data acquisition sequence, ECG and ventilation signals were used to coordinate optical data acquisition. Initially, the spectrometer was held in a standby mode. When the heart entered an iso-electric period, as determined by ECG, and the ventilator

was in a stable inspiration plateau, a trigger signal was sent to the spectrometer for diffuse reflectance signal acquisition. For fluorescent signal acquisition, the trigger signal was derived from the ventilation signal only, because it requires a long integration time (~ 1 second). Fig. 5-2 illustrates the concept of spectral data acquisition. The integration times were 50 ms and 700 ms for diffuse reflectance and fluorescent signals, respectively. For each measurement, five repeat fluorescence and diffuse reflectance spectra were taken and the mean spectrum was calculated and recorded accordingly. Please note that the diffuse reflectance and fluorescent signals were collected separately.

For preprocessing the recorded spectra, the dark baselines initially were subtracted from all the spectra. The acquired diffuse reflectance spectra were calibrated against a reflectance standard (FGS-20-02c, Avian Technologies, NH, USA). For the fluorescence spectra, a set of calibration factors derived using a calibrated light source (LS-1CAL, Ocean Optics, Dunedin, FL, USA) was used to remove all spectral alterations induced by the instruments. All pre-processed spectra were re-sampled to reduce spectral resolution to 2-nm.
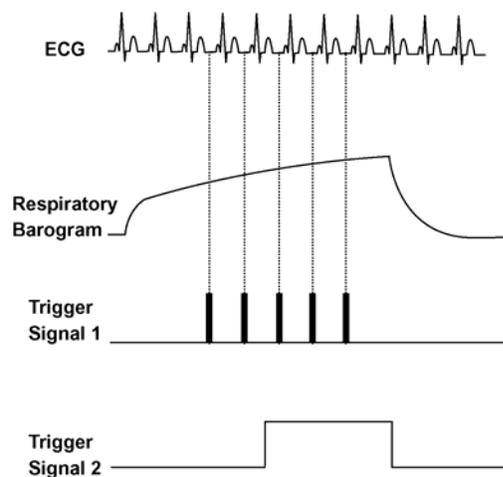
Figure 5-2. Synchronization of optical data acquisition with the ECG and ventilation signals. Trigger-signal 1 was used to initiate the acquisition of diffuse reflectance spectra; and Trigger-signal 2 to trigger the acquisition of fluorescence spectra.

5.2.4. *Histopathological examination*

Histopathological examination was performed by a pathologist, Dr. Robert Schmidt, to investigate the severity and extent of tissue injury, with the examination results used as the reference for spectral data grouping and comparison. Specimens from the optical-investigation sites were sectioned transversely and fixed in 10% neutral-buffered formalin. The tissue samples then were embedded in a paraffin block for staining. Two types of staining were used: hematoxylin and eosin (H&E) staining to demonstrate nuclear and cytoplasmic structures; and Masson's trichrome staining for connective tissues. Each section was examined by an experienced animal histologist, who quantitatively graded the severity of tissue injury within a specimen as 1 = minimal, 2 = mild, 3 = moderate or 4 = severe. The extent of tissue injury within a specimen also was graded, as 1 = focal, 2 = multifocal, 3 = multifocal to confluent, or 4 = diffuse.

5.2.5. *Spectral data analysis*

According to the histopathological features observed within each tissue specimen, spectral data were divided into different subsets to study the relationships between changes in optical spectra and histological abnormalities. From each spectral data subset, the mean spectra and their corresponding standard deviations were calculated to display spectral variations among the subsets. Spectral intensities at each wavelength were

compared between the subsets using statistical methods, including analysis of variance (ANOVA), as clarified below.

Furthermore, spectral interpretation algorithms (Chapter 3 and Chapter 4) were applied to the diffuse reflectance spectra to determine the hemodynamic parameters of the investigated sites. The spectral interpretation algorithms were developed based upon the spectral profile of hemoglobin (Hb), aiming to estimate Hb concentration and Hb oxygenation. Because Hb and myoglobin (Mb) have very similar absorption spectra in terms of spectral profiles, the algorithms were deemed to estimate the contributions from both Mb and Hb during this application. The concentration of Hb and Mb ([HbMb]) and oxygenation saturation of Hb and Mb ($SatO_2$) were treated as two additional factors for comparison between the subsets.

ANOVA was used to identify differences in indicative factors between the various tissue subsets identified. If the normality assumption was not met, non-parametric analysis (Kruskal-Wallis rank analysis of variance) was performed. For *post-hoc* analysis, Tukey's LSD was used to perform pair-wise multiple comparison procedures. Pearson product monument correlation analysis was used to investigate the correlation between the factors and histopathological scores within a subset. $P = 0.05$ was used as the threshold for statistical significance.

5.3. Results

A total of 14 rabbits were used for this study, with 12 of them surviving the first-stage of surgery. Excessive hemorrhage resulted in 2 rabbits during the second-stage surgery,

because of severe adhesion formation, and these two animals were excluded from further analysis. As a result, the data acquired from just 10 rabbits were analyzed.

5.3.1. Histopathological examination

The two most common histopathological characteristics observed in the infarcted rabbit hearts were (1) coagulative necrosis and (2) connective tissue proliferation. For this study, the definition of coagulative necrosis consisted of swelling and hyper-eosinophilia of myofibers, myofiber irregularity, and variable nuclear pyknosis (Fig. 5-3 (a) and Fig. 5-3 (b)). As coagulative necrosis progressed and became more severe, variable vacuolation (myocytolysis of myofibers – Fig. 5-3 (c)) appeared. As coagulative necrosis became more chronic, the vacuoles still could be seen in damaged fibers. Connective tissue proliferation could further be divided into two subcategories: loose connective tissue proliferation and dense connective tissue proliferation (Fig. 5-3 (d)). In this article, loose connective tissue proliferation primarily represents fibroblast proliferation and dispersed collagen fibers. Dense connective tissue proliferation indicates maturing of the lesion with considerably more densely arranged and compressed collagen. Some small and isolated atrophic fibers were found within areas of connective tissue proliferation (Fig. 5-3 (e)). Specimens that contained no coagulative necrosis or connective tissue proliferation were classified as healthy myocardium. In these specimens, minimal to moderate inflammatory cell infiltration, mostly with heterophils, occasionally was identified. These cells were found mostly within the epicardium or superficial myocardium, but also could be observed in deeper myocardial layers.

In general, the investigated sites that exhibited connective tissue proliferation were those in areas close to the ligature. The investigated sites with coagulative necrosis appeared in areas surrounding the infarct. The healthy sites were located farthest from the ligation site. All spectral measurements were divided into these 3 tissue subsets. Table 5-1 summarizes the population distribution of these three tissue subsets among the measurements and animal subjects. Eight measurements taken from areas that exhibited both coagulative necrosis and connective tissue proliferation were excluded from analysis.
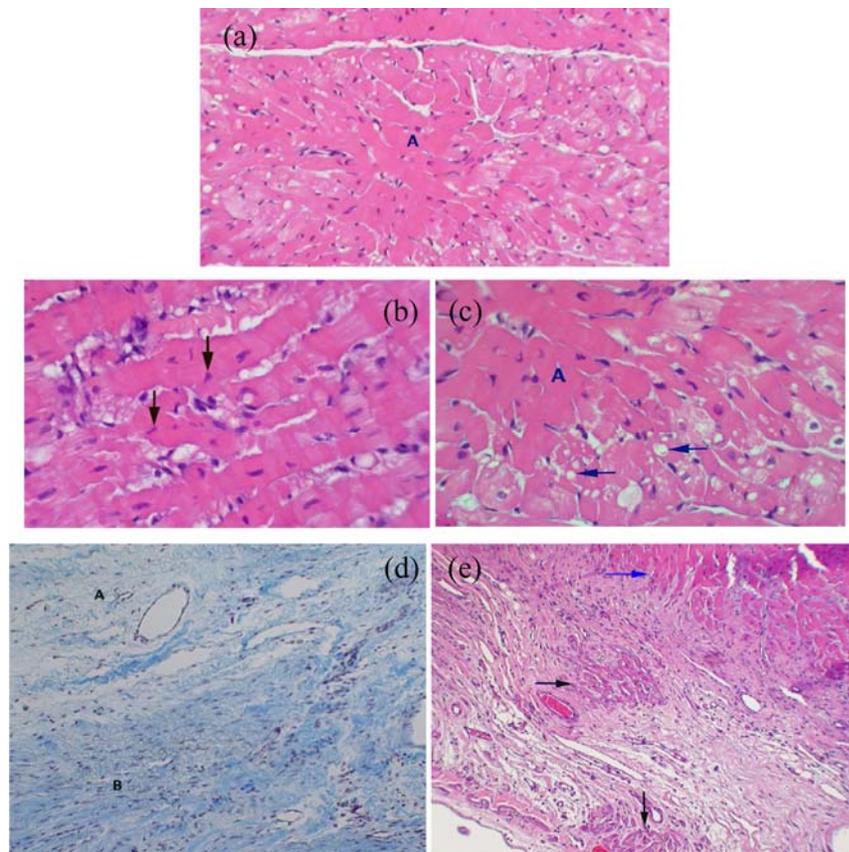
Figure 5-3. Histopathological features associated with myocardial infarction. (a) 25x H&E staining. Focus of coagulative necrosis 'A'. Note: hyper-eosinophilia, swelling, and irregularity of myofibers. (b) 100x H&E staining. Foci of granulative necrosis with pyknotic nuclei (arrow). Contraction bands also are present. (c) 100x H&E Focus of coagulative necrosis 'A' and vacuolation of associated myofibers (arrows). (d) 25x Masson's trichrome staining. Focus of myocardial fibrosis with more loosely

arranged fibers 'A' and dense connective tissue 'B'. (e) 25x H&E staining. Foci of myofiber atrophy. Minimal atrophy is noted at the edge of the connective tissue proliferation (blue arrow) and more sparsely atrophic foci also are present (black arrows).

Table 5-1. Population distribution of three subsets among the measurements and animal subjects

Animal ID	Number of measurements in each histopathological subsets		
	Connective tissue proliferation	Coagulative necrosis	Healthy tissue
1	8	6	0
2	14	0	4
3	10	4	2
4	9	0	4
5	4	6	11
6	7	4	2
7	7	10	2
8	11	4	2
9	6	4	6
10	10	4	2
Total	86	42	35

5.3.2. *Spectral data analysis*

The results of intensity analysis of diffuse reflectance spectra are shown in Fig 5-5 (a). In general, areas of connective tissue proliferation exhibited higher mean intensities than for healthy tissue or coagulative necrosis. Over the visible spectral region, the diffuse reflectance spectra mainly reflect the absorption properties of Hb and Mb. The intensity differences between connective tissue proliferation and coagulative necrosis were significant from 400 nm to 780 nm; the differences between connective tissue proliferation and healthy tissue significant from 400nm to 700 nm. In the longer wavelength region, the spectral profiles became flat with a slow descent. The spectral

profiles and mean intensities became similar for all three tissue types, with no statistically-significant differences detected.

Results for the intensity analysis of fluorescence spectra are illustrated in Fig. 5-5 (b). As shown in the figure, the spectra from all three tissue types comprised one major emission peak at 470 nm and two minor emission peaks at 390 nm and 600 nm. The fluorescence intensities from areas of connective tissue proliferation subset were significantly higher than those from the other two tissue types from 350 nm to 700 nm; they were about 3 times higher than healthy tissue at 390 nm, and 1.7 times higher at 470 nm and 600nm. Fluorescence intensities were not significantly different between healthy tissue and coagulative necrosis areas.
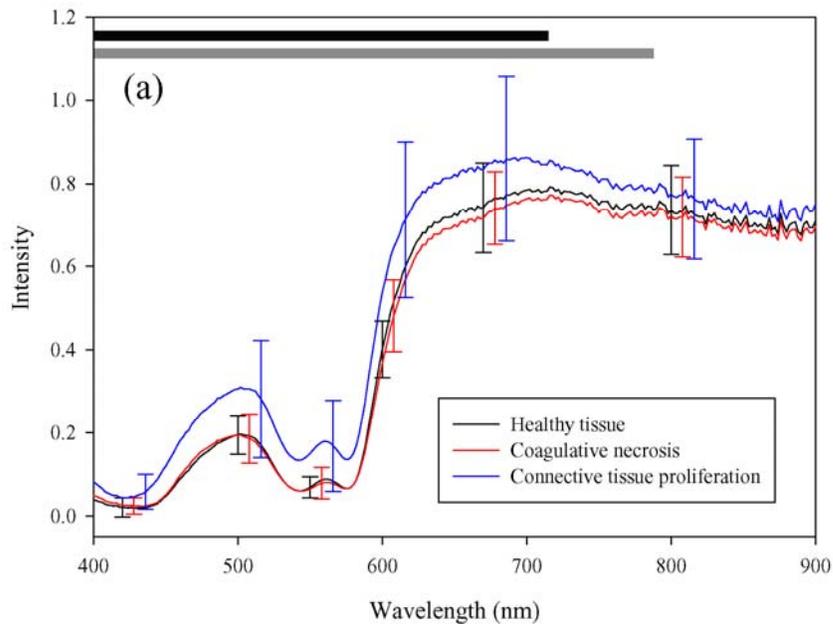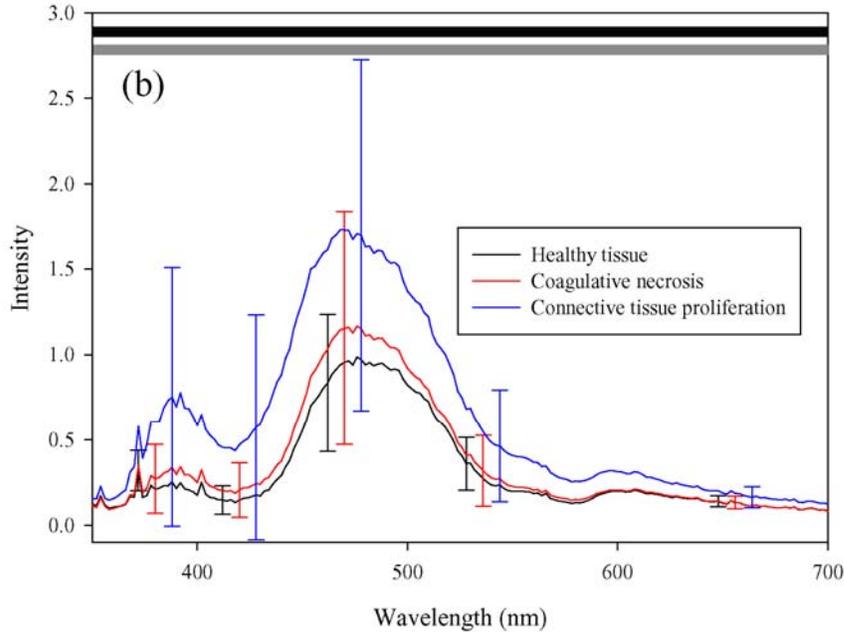
Figure 5-4. Optical spectra acquired during the second-stage surgery where (a) is diffuse reflectance spectra and (b) is fluorescence spectra. The solid lines represent the mean intensities for each subset and the error bars plot the corresponding standard deviations. The black bars indicate the spectral region where the mean intensities for healthy tissue and connective tissue proliferation are significantly different. The gray bar indicates the spectral region where the mean intensities for coagulative necrosis and connective tissue proliferation are significantly different.

Analysis of $SatO_2$ and [HbMb], estimated using spectral interpretation algorithms, is depicted in Fig. 5-5. As shown in Fig. 5-5 (a), connective tissue proliferation exhibited a significant higher mean $SatO_2$ level than the other two tissue types. The mean $SatO_2$ level was lower for coagulative necrosis than healthy tissue, but this difference was not statistically significant. Fig. 5-5 (b) shows how connective tissue had a significantly lower mean [HbMb] than the other two tissues. The mean [HbMb] levels in healthy tissue and coagulative necrosis were comparable.
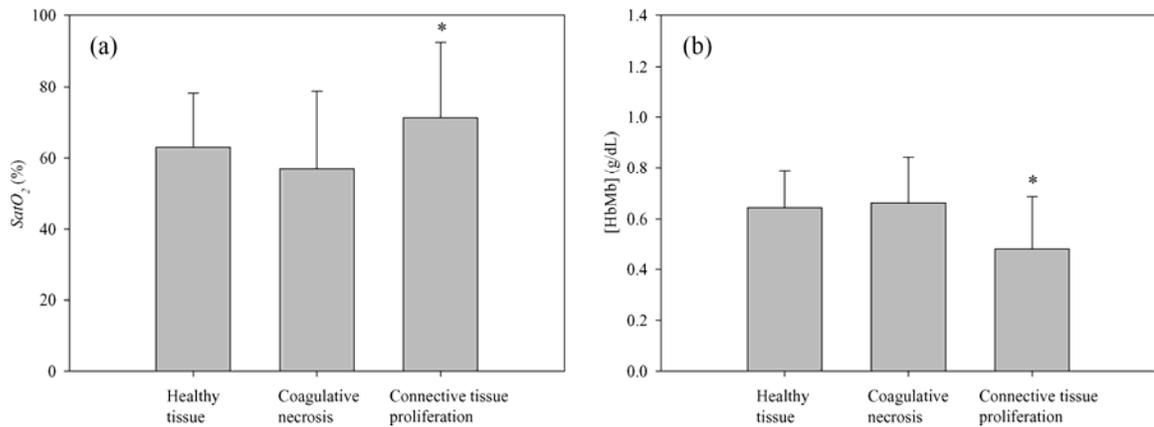
Figure 5-5. (a) Mean *SatO₂* levels and their corresponding standard deviations in the three tissue subsets. (b) Mean [HbMb] levels and their corresponding standard deviations in the three tissue subsets. Asterisks (*) indicate statistically significant differences (p<0.05) for connective tissue proliferation versus the other two tissue subsets.

The effects of the severity and extent of certain histopathological features on selected optical spectral features were investigated within individual tissue subset. Several representative wavelengths were chosen empirically (i.e., spectral factors) and their corresponding diffuse reflectance and fluorescence intensities compared against the histopathological scores to elucidate correlations. Table 5-2 summarizes the results of correlation analysis for connective tissue proliferation. All selected spectral factors were positively correlated with all histopathological scores except [HbMb], and 75% of the correlations were statistically significant. These correlations were especially pronounced for dense connective tissue proliferation. The significance of correlations also was more prominent for the extent versus severity of connective tissue proliferation. The results for the same analysis for coagulative necrosis are shown in Table 5-3. Here, correlations are mostly insignificant, except for a negative correlation between histopathological score and *SatO₂* level.

Table 5-2. Pearson correlation coefficients for spectral factors versus histopathological scores for connective tissue proliferation

Spectral Factors	Severity of loose connective tissue	Extent of loose connective tissue	Severity of dense connective tissue	Extent of dense connective tissue
Rd(504)	0.19	0.39*	0.24*	0.51*
Rd(560)	0.21	0.42*	0.26*	0.54*
Rd(686)	0.27*	0.39*	0.35*	0.51*
$SatO_2$	0.13	0.20	0.31*	0.29*
[HbMb]	-0.29*	-0.37*	-0.07	-0.40*
F(390)	0.27*	0.40*	0.27*	0.47*
F(470)	0.17	0.27*	0.14	0.40*
F(600)	0.28*	0.37*	0.21	0.47*

Rd(λ)= diffuse reflectance intensity at λ (nm), F(λ)= fluorescence intensity at λ (nm), * indicates $p<0.05$

Table 5-3. Pearson correlation coefficients for spectral factors and histopathological scores for coagulative necrosis

Spectral Factors	Severity of coagulative necrosis	Extent of coagulative necrosis
Rd(504)	0.04	0.02
Rd(560)	-0.01	-0.06
Rd(686)	-0.09	0.10
$SatO_2$	-0.32*	-0.33*
[HbMb]	-0.14	0.18
F(390)	-0.03	-0.06
F(470)	0.14	-0.10
F(600)	0.04	-0.18

Rd(λ)= diffuse reflectance intensity at λ (nm), F(λ)= fluorescence intensity at λ (nm), * indicates $p<0.05$

5.4. Discussion and conclusions

Two advantages of using a rabbit versus a rat model [90] are the rabbit's larger heart and thicker heart wall. The rabbit heart also is more similar than the rat's to the human heart, both morphologically and pathologically [16, 93], particularly in terms of insufficient

collateral coronary circulation [15]. In the previous study, we utilized visual observations as criteria by which to divide the spectral data for statistical comparisons [90]. In this study, a better reference, based upon histopathological features and scores, was used to evaluate the feasibility of using these optical methodologies for myocardial tissue diagnosis.

The histopathological examination provides detailed information about the type, extent and severity of a lesion. Coagulative necrosis usually occurs at an early stage of injury post MI, while connective tissue proliferation reveals the later development of scar tissue [16]. Most of the animal subjects exhibited both properties at the same time, which indicates the non-homogeneity of the healing process. Therefore, the local assessment of tissue condition becomes informative for further surgical treatment.

Spectral analysis across three histopathological tissue subests (healthy tissue, coagulative necrosis, and connective tissue proliferation) reveals connective tissue proliferation as statistically different than the other two conditions. These result are similar to those found in our previous study using rat hearts, 3 to 4 weeks post MI [90].

For diffuse reflectance spectra, statistically-significant differences in intensity occur in the spectral region where Hb and Mb exhibit dominant absorption. This indicates hemodynamic changes in areas with connective tissue proliferation. The $SatO_2$ and [HbMb] values estimated by the algorithms concur with this interpretation. Significantly higher mean $SatO_2$ and lower [HbMb] levels were discovered in areas with connective tissue proliferation. As mentioned in the Results section, areas with connective proliferation were identified close to the permanently-occluded coronary vessels, and the lower [HbMb] could be explained by the restricted blood flow into such areas. The

increased *SatO₂* levels could be due to less functional myocardium within scar tissue, which reduces energy and oxygen consumption, thereby generating higher *SatO₂* levels in Mb and Hb. The overall mean intensities of connective tissue proliferation were consistently higher than elsewhere. This phenomenon could be attributed to alterations in scattering properties, since proliferated connective tissue is rich in cross-linked fibrin, collagen and fibroblasts, all of which increase the scattering of light.

Within the spectral region of interest, intensity analysis of fluorescence spectra also found mean intensities for connective tissue proliferation being significantly higher than for the other two tissue conditions. There are several potential explanations for this increase in intensity. First, elastin and collagen are major components of connective tissue within the extracellular matrix. They also are fluorophores that generate an optimum emission wavelength of about 400 nm under 337 nm excitation [30]. More connective tissue proliferation in the tissue leads to a stronger emission peak around 390 nm. Second, under 337 nm, NDAD(P)H is another the major biological fluorophore that generates fluorescence emission at roughly 460 nm [30]. A lower metabolic rate can cause the accumulation of NAD(P)H; hence, the elevation of fluorescence intensities. Because the proliferation of connective tissue alters the structure of the intra-cellular matrix and isolates viable myocardium, despite the higher *SatO₂* level in Mb/Hb in fibrosed areas, this alteration in structure may impede the diffusion of oxygen to distant viable myocardium [94], resulting in suppressed metabolism. Third, within the visible spectral region, the reduced [HbMb] in fibrosed areas reduces the absorption of both excitation and emission light. These combined effects can further enhance fluorescence intensities. Finally, due to structural alterations, the scattering properties of the tissue is

modified as well, potentially shortening the optical path-length for the excitation/emission light and boosting the intensities of fluorescence.

Within areas of connective tissue proliferation, spectral factors and histopathological scores were significantly correlated. As expected when the extent and severity of a lesion increase, except [HbMb], all the spectral factors tended to rise. This result implies that the proposed optical methodology is not only able to differentiate between lesion types, but also to grade them. On average, the correlations between spectral factors and dense connective tissue were stronger than those between spectral factors and loose connective tissue, in terms of both injury extent and severity. This may indicate that dense connective tissue proliferation exerts a greater influence upon the optical spectrum than loose connective tissue. For coagulative necrosis, the only significant correlation was a negative one, between $SatO_2$ levels and histopathology scores. This phenomenon corresponds with hypoxia being a major cause of cell death post MI.

Using the fiber-optic based system described in this paper, one major hurdle is the motion of the beating heart. Motion artifacts can alter contact location and pressure during optical measurements. This issue might cause unwanted variations in optical signals. To reduce this effect, repeated measurements were taken. Moreover, the proposed gating mechanism using ECG and ventilation signals significantly reduced the percentage standard deviation (i.e., standard deviation/mean); on average, the percentage standard deviation was reduced by two-third over the entire spectrum [95]. A previous study determined that the probe pressure used in this study should not alter optical signals

significantly [63]. Therefore, we believe that the spectral variations we observed should mainly be attributed to differences in tissue characteristics.

In summary, the results contained herein argue for the feasibility and applicability of the proposed optical methodology using combined diffuse reflectance spectroscopy and fluorescence spectroscopy for MI tissue diagnosis. Spectral analysis of diffuse reflectance and fluorescence spectra indicate that myocardium with connective tissue proliferation can be differentiated from other tissue states. Moreover, the magnitudes of the extracted spectral factors can be used to grade lesion severity.

6. Summary

In the first portion of the study, a new algorithm was derived to estimate hemoglobin (Hb) oxygenation ($SatO_2$) from diffuse reflectance spectra. The algorithm was developed based on the unique spectral profile differences between the extinction coefficient spectra of oxy-Hb and deoxy-Hb within the visible wavelength region. Using differential wavelet transformation, these differences were quantified using the locations of certain spectral features, and, then, they were related to the oxygenation saturation level of Hb. The applicability of the algorithm was evaluated using a set of diffuse reflectance spectra produced by a Monte Carlo simulation model of photon migration and was applied to the diffuse reflectance spectra acquired from *in vivo* experiments to demonstrate its clinical utility. The validation results concluded that the algorithm is applicable to various tissue types (i.e., scattering properties) and can be used in conjunction with a diverse range of probe geometries for real-time monitoring of Hb oxygenation.

The second portion of the study introduces a new algorithm to retrieve regional hemoglobin concentrations ([Hb]) information from diffuse reflectance spectra. The proposed algorithm utilizes the natural logarithmic operation and the differential wavelet transform to effectively quench the scattering and excitation intensity effects on diffuse reflectance spectra, and then employs the concept of isosbestic wavelength in the transformed spectra to reduce the effects of hemoglobin oxygenation. As the result, the intensity at the defined isosbestic wavelength of the transformed spectra is a good indicator of [Hb] estimation. The algorithm was derived and validated using theoretical

spectra produced by Monte Carlo simulations of photon migration. Its accuracy was further evaluated using liquid tissue phantoms, and its clinical utility with an *in vivo* clinical study of brain tumors. The results demonstrate the applicability of the algorithm for real-time [Hb] estimations from diffuse reflectance spectra, acquired by means of a fiber-optic spectroscopy system.

The final portion of the study aims to evaluate the applicability of utilizing diffuse reflectance spectroscopy and fluorescence spectroscopy as an intraoperative guidance tool for diagnosing myocardial infarction (MI). A rabbit model of MI, induced via ligation of a major coronary artery of the left ventricle, was used. Three to four weeks after MI induction, the severity and extent of myocardial tissue injury were investigated by both histological examination and the proposed spectroscopic methodology. A fiber-optic spectroscopy system was employed to collect fluorescence signals at 337 nm excitation and diffuse reflectance signals between 400 nm and 900 nm. During spectral data acquisition, a gating mechanism using electrocardiogram and ventilation signals was designed to reduce motion artifacts. The spectral data were divided into different subsets, assigned according to the histopathological features of the under-lying tissue, so as to identify lesion-specific spectral alterations. Analysis of both diffuse reflectance spectra and fluorescence spectra indicate that the connective tissue proliferation that occurs post MI induces significant spectral alterations. The magnitude of these alterations can be used to grade each lesion quantitatively.

LIST OF REFERENCES

1.   W. Rosamond, K. Flegal, K. Furie, A. Go, K. Greenlund, N. Haase, S. M. Hailpern, M. Ho, V. Howard, B. Kissela, S. Kittner, D. Lloyd-Jones, M. McDermott, J. Meigs, C. Moy, G. Nichol, C. O'Donnell, V. Roger, P. Sorlie, J. Steinberger, T. Thom, M. Wilson, and Y. Hong, "Heart disease and stroke statistics--2008 update: a report from the American Heart Association Statistics Committee and Stroke Statistics Subcommittee," Circulation **117**, e25-146 (2008).

2.   W. C. Stanley, "Changes in cardiac metabolism: a critical step from stable angina to ischaemic cardiomyopathy," Eur Heart J Suppl **3**, O2-7 (2001).

3.   J. W. Hurst, V. Fuster, R. A. O'Rourke, R. A. Walsh, and P. Poole-Wilson, *Hurst's the Heart,* 12 ed. (McGraw-Hill Professional, 2007), p. 2477.

4.   K. A. Reimer and R. B. Jennings, "The "wavefront phenomenon" of myocardial ischemic cell death. II. Transmural progression of necrosis within the framework of ischemic bed size (myocardium at risk) and collateral flow," Lab Invest **40**, 633-644 (1979).

5.   G. Majno and I. Joris, "Apoptosis, oncosis, and necrosis. An overview of cell death," Am J Pathol **146**, 3-15 (1995).

6.   L. M. Buja, "Myocardial ischemia and reperfusion injury," Cardiovasc Pathol **14**, 170-175 (2005).

7.   L. M. Buja and M. L. Entman, "Modes of myocardial cell injury and cell death in ischemic heart disease," Circulation **98**, 1355-1357 (1998).

8.   W. M. Blankesteijn, E. Creemers, E. Lutgens, J. P. Cleutjens, M. J. Daemen, and J. F. Smits, "Dynamics of cardiac wound healing following myocardial infarction: observations in genetically altered mice," Acta Physiol Scand **173**, 75-82 (2001).

9.   M. C. Fishbein, D. Maclean, and P. R. Maroko, "The histopathologic evolution of myocardial infarction," Chest **73**, 843-849 (1978).

10.   J. E. Jordan, Z.-Q. Zhao, and J. Vinten-Johansen, "The role of neutrophils in myocardial ischemia-reperfusion injury," Cardiovasc Res **43**, 860-878 (1999).

11.   R. Virmani, A. Burke, A. Farb, and J. B. Atkinson, *Cardiovascular Pathology* 2ed. (WB Saunders, Philadephia, 2001), Vol. 40.

12.   E. J. Battegay, "Angiogenesis: mechanistic insights, neovascular diseases, and therapeutic prospects," J Mol Med **73**, 333-346 (1995).

13. I. E. Willems, M. G. Havenith, J. G. De Mey, and M. J. Daemen, "The alpha-smooth muscle actin-positive cells in healing human myocardial scars," Am J Pathol **145**, 868-875 (1994).

14. A. M. Gallagher, T. D. Bahnson, H. Yu, N. N. Kim, and M. P. Printz, "Species variability in angiotensin receptor expression by cultured cardiac fibroblasts and the infarcted heart," Am J Physiol **274**, H801-809 (1998).

15. M. P. Maxwell, D. J. Hearse, and D. M. Yellon, "Species variation in the coronary collateral circulation during regional myocardial ischaemia: a critical determinant of the rate of evolution and extent of myocardial infarction," Cardiovasc Res **21**, 737-746 (1987).

16. C. Morales, G. E. Gonzalez, M. Rodriguez, C. A. Bertolasi, and R. J. Gelpi, "Histopathologic time course of myocardial infarct in rabbit hearts," Cardiovasc Pathol **11**, 339-345 (2002).

17. R. Richards-Kortum and E. Sevick-Muraca, "Quantitative optical spectroscopy for tissue diagnosis," Annual Review of Physical Chemistry **47**, 555-606 (1996).

18. W. C. Lin, S. A. Toms, M. Johnson, E. D. Jansen, and A. Mahadevan-Jansen, "In vivo brain tumor demarcation using optical spectroscopy," Photochem Photobiol **73**, 396-402 (2001).

19. K. Sokolov, M. Follen, and R. Richards-Kortum, "Optical spectroscopy for detection of neoplasia," Curr Opin Chem Biol **6**, 651-658 (2002).

20. D. J. Parekh, L. W. Chiang, and S. D. Herrell, "In vivo assessment of radio frequency induced thermal damage of kidney using optical spectroscopy," J Urol **176**, 1626-1630 (2006).

21. S. A. Toms, W. C. Lin, R. J. Weil, M. D. Johnson, E. D. Jansen, and A. Mahadevan-Jansen, "Intraoperative optical spectroscopy identifies infiltrating glioma margins with high sensitivity," Neurosurgery **61**, 327-335; discussion 335-326 (2007).

22. S. Bhatia, J. Ragheb, M. Johnson, S. Oh, D. I. Sandberg, and W. C. Lin, "The role of optical spectroscopy in epilepsy surgery in children," Neurosurg Focus **25**, E24 (2008).

23. L. V. Wang and H.-i. Wu, *Biomedical optics: principles and imaging* (Wiley-Interscience, 2007).

24. S. Schuder, J. B. Wittenberg, B. Haseltine, and B. A. Wittenberg, "Spectrophotometric determination of myoglobin in cardiac and skeletal muscle: separation from hemoglobin by subunit-exchange chromatography," Anal Biochem **92**, 473-481 (1979).

25.   E. Haggblad, T. Lindbergh, M. G. Karlsson, H. Casimir-Ahn, E. G. Salerud, and T. Stromberg, "Myocardial tissue oxygenation estimated with calibrated diffuse reflectance spectroscopy during coronary artery bypass grafting," J Biomed Opt **13**, 054030 (2008).

26.   A. A. Stratonnikov and V. B. Loschenov, "Evaluation of blood oxygen saturation in vivo from diffuse reflectance spectra," J Biomed Opt **6**, 457-467 (2001).

27.   A. E. Arai, C. E. Kasserra, P. R. Territo, A. H. Gandjbakhche, and R. S. Balaban, "Myocardial oxygenation in vivo: optical spectroscopy of cytoplasmic myoglobin and mitochondrial cytochromes," Am J Physiol **277**, H683-697 (1999).

28.   S. C. Gebhart, W. C. Lin, and A. Mahadevan-Jansen, "In vitro determination of normal and neoplastic human brain tissue optical properties using inverse adding-doubling," Phys Med Biol **51**, 2011-2027 (2006).

29.   P. R. Bargo, S. A. Prahl, T. T. Goodell, R. A. Sleven, G. Koval, G. Blair, and S. L. Jacques, "In vivo determination of optical properties of normal and tumor tissue with white light reflectance and an empirical light transport model during endoscopy," J Biomed Opt **10**, 034018 (2005).

30.   N. Ramanujam, "Fluorescence Spectroscopy In Vivo," in *Encyclopedia of Analytical Chemistry*, R. A. Meyers, ed. (John Wiley & Sons Ltd, Chichester, 2000), pp. pp. 20–56.

31.   S. Andersson-Engels, C. Klinteberg, K. Svanberg, and S. Svanberg, "In vivo fluorescence imaging for tissue diagnostics," Phys Med Biol **42**, 815-824 (1997).

32.   K. A. Horvath, K. T. Schomacker, C. C. Lee, and L. H. Cohn, "Intraoperative myocardial ischemia detection with laser-induced fluorescence," J Thorac Cardiovasc Surg **107**, 220-225 (1994).

33.   G. E. Kochiadakis, S. I. Chrysostomakis, M. D. Kalebubas, G. M. Filippidis, I. G. Zacharakis, T. G. Papazoglou, and P. E. Vardas, "The role of laser-induced fluorescence in myocardial tissue characterization: an experimental in vitro study," Chest **120**, 233-239 (2001).

34.   C. D. Anderson, W. C. Lin, J. Beckham, A. Mahadevan-Jansen, C. R. Buttemere, J. Pierce, I. B. Nicoud, C. Wright Pinson, and R. S. Chari, "Fluorescence spectroscopy accurately detects irreversible cell damage during hepatic radiofrequency ablation," Surgery **136**, 524-531 (2004).

35.   G. K. Lund, A. Stork, M. Saeed, M. P. Bansmann, J. H. Gerken, V. Muller, J. Mester, C. B. Higgins, G. Adam, and T. Meinertz, "Acute myocardial infarction: evaluation with first-pass enhancement and delayed enhancement MR imaging compared with 201Tl SPECT imaging," Radiology **232**, 49-57 (2004).

36. J. J. Bax, B. L. van Eck-Smit, and E. E. van der Wall, "Assessment of tissue viability: clinical demand and problems," Eur Heart J **19**, 847-858 (1998).

37. B. L. Gerber, J. Garot, D. A. Bluemke, K. C. Wu, and J. A. Lima, "Accuracy of contrast-enhanced magnetic resonance imaging in predicting improvement of regional myocardial function in patients after acute myocardial infarction," Circulation **106**, 1083-1089 (2002).

38. G. A. Krombach, M. F. Wendland, C. B. Higgins, and M. Saeed, "MR imaging of spatial extent of microvascular injury in reperfused ischemically injured rat myocardium: value of blood pool ultrasmall superparamagnetic particles of iron oxide," Radiology **225**, 479-486 (2002).

39. M. F. Wendland, M. Saeed, G. Lund, and C. B. Higgins, "Contrast-enhanced MRI for quantification of myocardial viability," J Magn Reson Imaging **10**, 694-702 (1999).

40. R. M. Bateman, M. D. Sharpe, and C. G. Ellis, "Bench-to-bedside review: microvascular dysfunction in sepsis--hemodynamics, oxygen transport, and nitric oxide," Crit Care **7**, 359-373 (2003).

41. M. Siegemund, J. van Bommel, and C. Ince, "Assessment of regional tissue oxygenation," Intensive Care Med **25**, 1044-1060 (1999).

42. D. A. Benaron, I. H. Parachikov, S. Friedland, R. Soetikno, J. Brock-Utne, P. J. van der Starre, C. Nezhat, M. K. Terris, P. G. Maxim, J. J. Carson, M. K. Razavi, H. B. Gladstone, E. F. Fincher, C. P. Hsu, F. L. Clark, W. F. Cheong, J. L. Duckworth, and D. K. Stevenson, "Continuous, noninvasive, and localized microvascular tissue oximetry using visible light spectroscopy," Anesthesiology **100**, 1469-1475 (2004).

43. C. Verdant and D. De Backer, "How monitoring of the microcirculation may help us at the bedside," Curr Opin Crit Care **11**, 240-244 (2005).

44. H. Knotzer and W. R. Hasibeder, "Microcirculatory function monitoring at the bedside--a view from the intensive care," Physiol Meas **28**, R65-86 (2007).

45. R. Mallia, S. S. Thomas, A. Mathews, R. Kumar, P. Sebastian, J. Madhavan, and N. Subhash, "Oxygenated hemoglobin diffuse reflectance ratio for in vivo detection of oral pre-cancer," J Biomed Opt **13**, 041306 (2008).

46. H. W. Wang, J. K. Jiang, C. H. Lin, J. K. Lin, G. J. Huang, and J. S. Yu, "Diffuse reflectance spectroscopy detects increased hemoglobin concentration and decreased oxygenation during colon carcinogenesis from normal to malignant tumors," Opt Express **17**, 2805-2817 (2009).

47.   L. J. Brown, "A new instrument for the simultaneous measurement of total hemoglobin, % oxyhemoglobin, % carboxyhemoglobin, % methemoglobin, and oxygen content in whole blood," IEEE Trans Biomed Eng **27**, 132-138 (1980).

48.   W. T. Knoefel, N. Kollias, D. W. Rattner, N. S. Nishioka, and A. L. Warshaw, "Reflectance spectroscopy of pancreatic microcirculation," J Appl Physiol **80**, 116-123 (1996).

49.   M. H. Smith, K. R. Denninghoff, A. Lompado, and L. W. Hillman, "Effect of multiple light paths on retinal vessel oximetry," Appl Opt **39**, 1183-1193 (2000).

50.   M. Kohl, U. Lindauer, G. Royl, M. Kuhl, L. Gold, A. Villringer, and U. Dirnagl, "Physical model for the spectroscopic analysis of cortical intrinsic optical signals," Phys Med Biol **45**, 3749-3764 (2000).

51.   M. Hammer, E. Thamm, and D. Schweitzer, "A simple algorithm for in vivo ocular fundus oximetry compensating for non-haemoglobin absorption and scattering," Phys Med Biol **47**, N233-238 (2002).

52.   J. Gade, D. Palmqvist, P. Plomgard, and G. Greisen, "Diffuse reflectance spectrophotometry with visible light: comparison of four different methods in a tissue phantom," Phys Med Biol **51**, 121-136 (2006).

53.   R. M. Doornbos, R. Lang, M. C. Aalders, F. W. Cross, and H. J. Sterenborg, "The determination of in vivo human tissue optical properties and absolute chromophore concentrations using spatially resolved steady-state diffuse reflectance spectroscopy," Phys Med Biol **44**, 967-981 (1999).

54.   G. M. Palmer, C. Zhu, T. M. Breslin, F. Xu, K. W. Gilchrist, and N. Ramanujam, "Monte Carlo-based inverse model for calculating tissue optical properties. Part II: Application to breast cancer diagnosis," Appl Opt **45**, 1072-1078 (2006).

55.   R. Reif, O. A'Amar, and I. J. Bigio, "Analytical model of light reflectance for extraction of the optical properties in small volumes of turbid media," Appl Opt **46**, 7317-7328 (2007).

56.   S. Mallat, "Zero-crossings of a wavelet transform," IEEE Trans. Inform. Theory **37**, 1019-1033 (1991).

57.   A. M. Nilsson, C. Sturesson, D. L. Liu, and S. Andersson-Engels, "Changes in spectral shape of tissue optical properties in conjunction with laser-induced thermotherapy," Appl Opt **37**, 1256-1267 (1998).

58.   V. V. Tuchin, *Tissue optics: light scattering methods and instruments for medical diagnosis,* 2 ed. (SPIE, Bellingham, 2007).

59. L. Wei-Chiang, I. S. David, B. Sanjiv, J. Mahlon, O. Sanghoon, and R. John, "Diffuse reflectance spectroscopy for in vivo pediatric brain tumor detection," Journal of Biomedical Optics **15**, 061709 (2010).

60. A. Jubran, "Pulse oximetry," Crit Care **3**, R11-R17 (1999).

61. N. T. Evans and P. F. Naylor, "The oxygen tension gradient across human epidermis," Respir Physiol **3**, 38-42 (1967).

62. B. Meyer, C. Schaller, C. Frenkel, B. Ebeling, and J. Schramm, "Distributions of local oxygen saturation and its response to changes of mean arterial blood pressure in the cerebral cortex adjacent to arteriovenous malformations," Stroke **30**, 2623-2630 (1999).

63. Y. Ti and W. C. Lin, "Effects of probe contact pressure on in vivo optical spectroscopy," Opt Express **16**, 4250-4262 (2008).

64. R. L. Jensen, "Brain tumor hypoxia: tumorigenesis, angiogenesis, imaging, pseudoprogression, and as a therapeutic target," J Neurooncol **92**, 317-335 (2009).

65. S. Mallat, *A Wavelet Tour of Signal Processing* (Academic Press, London, 1999).

66. D. De Backer, J. Creteur, J. C. Preiser, M. J. Dubois, and J. L. Vincent, "Microvascular blood flow is altered in patients with sepsis," Am J Respir Crit Care Med **166**, 98-104 (2002).

67. H. W. Wang, T. C. Zhu, M. E. Putt, M. Solonenko, J. Metz, A. Dimofte, J. Miles, D. L. Fraker, E. Glatstein, S. M. Hahn, and A. G. Yodh, "Broadband reflectance measurements of light penetration, blood oxygenation, hemoglobin concentration, and drug concentration in human intraperitoneal tissues before and after photodynamic therapy," J Biomed Opt **10**, 14004 (2005).

68. J. Lee, D. J. Saltzman, A. E. Cerussi, D. V. Gelfand, J. Milliken, T. Waddington, B. J. Tromberg, and M. Brenner, "Broadband diffuse optical spectroscopy measurement of hemoglobin concentration during hypovolemia in rabbits," Physiol Meas **27**, 757-767 (2006).

69. J. E. Bender, A. B. Shang, E. W. Moretti, B. Yu, L. M. Richards, and N. Ramanujam, "Noninvasive monitoring of tissue hemoglobin using UV-VIS diffuse reflectance spectroscopy: a pilot study," Opt Express **17**, 23396-23409 (2009).

70. H. Rabe, N. Stupp, M. Ozgun, E. Harms, and H. Jungmann, "Measurement of transcutaneous hemoglobin concentration by noninvasive white-light spectroscopy in infants," Pediatrics **116**, 841-843 (2005).

71.	J. C. Finlay and T. H. Foster, "Hemoglobin oxygen saturations in phantoms and in vivo from measurements of steady-state diffuse reflectance at a single, short source-detector separation," Med Phys **31**, 1949-1959 (2004).

72.	N. Rajaram, T. H. Nguyen, and J. W. Tunnell, "Lookup table-based inverse model for determining optical properties of turbid media," J Biomed Opt **13**, 050501 (2008).

73.	D. A. Benaron, I. H. Parachikov, W. F. Cheong, S. Friedland, B. E. Rubinsky, D. M. Otten, F. W. Liu, C. J. Levinson, A. L. Murphy, J. W. Price, Y. Talmi, J. P. Weersing, J. L. Duckworth, U. B. Horchner, and E. L. Kermit, "Design of a visible-light spectroscopy clinical tissue oximeter," J Biomed Opt **10**, 44005 (2005).

74.	L. S. L. Arakaki, M. J. Kushmerick, and D. H. Burns, "Myoglobin Oxygen Saturation Measured Independently of Hemoglobin in Scattering Media by Optical Reflectance Spectroscopy," Appl. Spectrosc **50**, 697-707 (1996).

75.	S. G. Mallat, "A theory for multiresolution signal decomposition: the wavelet representation," Pattern Analysis and Machine Intelligence, IEEE Transactions on **11**, 674-693 (1989).

76.	S. Mallat and S. Zhong, "Characterization of signals from multiscale edges," Pattern Analysis and Machine Intelligence, IEEE Transactions on **14**, 710-732 (1992).

77.	S. Mallat and W. L. Hwang, "Singularity detection and processing with wavelets," IEEE Trans. Inform. Theory **38**, 617-643 (1992).

78.	S. Prahl, Mie Scattering Calculator, http://omlc.ogi.edu/calc/mie_calc.html.

79.	P. R. Dallman, G. D. Barr, C. M. Allen, and H. R. Shinefield, "Hemoglobin concentration in white, black, and Oriental children: is there a need for separate criteria in screening for anemia?," Am J Clin Nutr **31**, 377-380 (1978).

80.	A. A. Lammertsma, D. J. Brooks, R. P. Beaney, D. R. Turton, M. J. Kensett, J. D. Heather, J. Marshall, and T. Jones, "In vivo measurement of regional cerebral haematocrit using positron emission tomography," J Cereb Blood Flow Metab **4**, 317-322 (1984).

81.	K. Kuppusamy, W. Lin, G. R. Cizek, and E. M. Haacke, "In vivo regional cerebral blood volume: quantitative assessment with 3D T1-weighted pre- and postcontrast MR imaging," Radiology **201**, 106-112 (1996).

82.	K. L. Leenders, D. Perani, A. A. Lammertsma, J. D. Heather, P. Buckingham, M. J. Healy, J. M. Gibbs, R. J. Wise, J. Hatazawa, S. Herold, and et al., "Cerebral

blood flow, blood volume and oxygen utilization. Normal values and effect of age," Brain **113 (Pt 1)**, 27-47 (1990).

83. U. Sabatini, P. Celsis, G. Viallard, A. Rascol, and J. P. Marc-Vergnes, "Quantitative assessment of cerebral blood volume by single-photon emission computed tomography," Stroke **22**, 324-330 (1991).

84. W. Y. Kim and H. Y. Lee, "Brain angiogenesis in developmental and pathological processes: mechanism and therapeutic intervention in brain tumors," Febs J **276**, 4653-4664 (2009).

85. D. Lloyd-Jones, R. J. Adams, T. M. Brown, M. Carnethon, S. Dai, G. De Simone, T. B. Ferguson, E. Ford, K. Furie, C. Gillespie, A. Go, K. Greenlund, N. Haase, S. Hailpern, P. M. Ho, V. Howard, B. Kissela, S. Kittner, D. Lackland, L. Lisabeth, A. Marelli, M. M. McDermott, J. Meigs, D. Mozaffarian, M. Mussolino, G. Nichol, V. L. Roger, W. Rosamond, R. Sacco, P. Sorlie, V. L. Roger, T. Thom, S. Wasserthiel-Smoller, N. D. Wong, and J. Wylie-Rosett, "Heart disease and stroke statistics--2010 update: a report from the American Heart Association," Circulation **121**, e46-e215 (2010).

86. G. Ertl and S. Frantz, "Wound model of myocardial infarction," Am J Physiol Heart Circ Physiol **288**, H981-983 (2005).

87. T. Lindbergh, E. Haggblad, H. Ahn, E. Goran Salerud, M. Larsson, and T. Stromberg, "Improved model for myocardial diffuse reflectance spectra by including mitochondrial cytochrome aa3, methemoglobin, and inhomogenously distributed RBC," J Biophotonics (2010).

88. K. A. Schenkman, D. R. Marble, D. H. Burns, and E. O. Feig, "Optical Spectroscopic Method for in Vivo Measurement of Cardiac Myoglobin Oxygen Saturation," Appl. Spectrosc. **53**, 332-338 (1999).

89. E. Gussakovsky, O. Jilkina, Y. Yang, and V. Kupriyanov, "Hemoglobin plus myoglobin concentrations and near infrared light pathlength in phantom and pig hearts determined by diffuse reflectance spectroscopy," Anal Biochem **382**, 107-115 (2008).

90. Y. Ti, P. Chen, and W. C. Lin, "In vivo characterization of myocardial infarction using fluorescence and diffuse reflectance spectroscopy," J Biomed Opt **15**, 037009 (2010).

91. B. Podesser, G. Wollenek, R. Seitelberger, H. Siegel, E. Wolner, W. Firbas, and M. Tschabitscher, "Epicardial branches of the coronary arteries and their distribution in the rabbit heart: the rabbit heart as a model of regional ischemia," Anat Rec **247**, 521-527 (1997).

92.   B. H. Lee, W. H. Kim, M. J. Choi, J. R. Rho, and W. G. Kim, "Chronic heart failure model in rabbits based on the concept of the bifurcation/trifurcation coronary artery branching pattern," Artif Organs **26**, 360-365 (2002).

93.   B. Z. Atkins, C. W. Lewis, W. E. Kraus, K. A. Hutcheson, D. D. Glower, and D. A. Taylor, "Intracardiac transplantation of skeletal myoblasts yields two populations of striated cells in situ," Ann Thorac Surg **67**, 124-129 (1999).

94.   R. A. F. Clark, *The molecular and cellular biology of wound repair,* 2 ed. (Plenum Press, New York, 1996).

95.   P. Chen, Y. Ti, and W. Lin, "In vivo Characterization of Myocardial Infarct Using Optical Spectroscopy," in Biomedical Optics, OSA Technical Digest (CD) (Optical Society of America, 2010), paper BSuD66 (2010).

VITA

PO-CHING CHEN

Born, Taipei, Taiwan

2002	Bachelor of Science in Electrical Engineering Yuan Ze University Taiwan
2003-2006	Research Assistant Biophysics Laboratory Taipei Veterans General Hospital Taiwan
2006-2008	Graduate Assistant, Research Assistant Department of Biomedical Engineering Florida International University Miami, Florida
2009-2011	Dissertation Year Fellow University Graduate School Florida International University Miami, Florida

PRESENTATIONS AND PUBLICATIONS

Chen, Po-Ching, Lee, Steven and Kuo, Cheng-Deng, "Delineation of T Wave in ECG by Wavelet Transform Using Multiscale Differential Operator," IEEE Trans. Biomed. Eng. 53, 1429-1433 (2006).

Chen, Po-Ching, "In Vivo Real-Time Assessment of Post-Infarction Myocardial Injury Using A Multimodal Spectral Imaging System, " Biomedical Research Initiative Student Summer Research Award in Biomedical Science, MBRS, Florida International University, (2007).

Chen, Po-Ching and Lin, Wei-Chiang, "Real-time assessment of infarction induced myocardial injury using a multi-modal spectral imaging system," Biomedical and Comparative Immunology Symposium, Florida International University, Miami, FL, March 8th, (2008).

Chen, Po-Ching, Ti, Yalin, Fernald, Bradley, Oh, Sanghoon, and Lin, Wei-Chiang, "In vivo optical characterization of myocardial injury induced by infarction," NIH Inter-

Institute Workshop on Optical Diagnostic and Biophotonic Methods from Bench to Bedside, National Institutes of Health, Bethesda, MD, October 2nd, (2009).

Chen, Po-Ching, Ti, Yalin, and Lin, Wei-Chiang, "In vivo Characterization of Myocardial Infarct Using Optical Spectroscopy," in Biomedical Optics, OSA Technical Digest (CD) (Optical Society of America, 2010), paper BSuD66 (2010).

Chen, Po-Ching and Lin, Wei-Chiang, "Determination of in vivo Blood Oxygen Saturation and Blood Volume Fraction Using Diffuse Reflectance Spectroscopy," IFMBE Proceedings 32, 336-339 (2010).

Lin, Wei-Chiang, Ti, Yalin, and Chen, Po-Ching, "In vivo pathophysiological characterization of myocardial infarction," BioTech 2009 - EDC's 8th Annual Life Science Conference, Hyatt Regency, Miami, FL, April 30th, (2009).

Ti, Yalin, Chen, Po-Ching, and Lin, Wei-Chiang, "In vivo characterization of myocardial infarction using fluorescence and diffuse reflectance spectroscopy," J Biomed Opt 15, 037009 (2010).

Po-Ching Chen and Wei-Chiang Lin, "Spectral-profile-based algorithm for hemoglobin oxygen saturation determination from diffuse reflectance spectra," Biomed Opt Express 2, 1082-1096 (2011).